Retrieval of UV-Visible aerosol absorption using AERONET and OMI-MODIS synergy: Spatial and temporal variability across major aerosol environments

Vinay Kayetha[1,2], Omar Torres[2], Hiren Jethva[2,3]

5   [1]Science Systems and Applications Inc., Lanham, Maryland-20706, USA
[2]NASA Goddard Space Flight Center, Greenbelt, Maryland-20771, USA
[3]Universities Space Research Association, Columbia, Maryland-21046, USA

Correspondence to: Vinay Kayetha (vinay.k.kayetha@nasa.gov)

10   **Abstract.** Measuring spectral aerosol absorption remains a challenging task in aerosol studies, especially in the UV region, where the ground and airborne measurements are sparse. In this research, we introduce an algorithm that synergizes ground measurements with satellite observations for the derivation of spectral single scattering albedo (SSA, ω_o) of aerosols in the UV to visible range (340-670 nm). The approach consists in explaining satellite measured near-UV radiances (340, 354 and 388 nm) by the Ozone Monitoring Instrument (OMI), and

15   visible radiances (466 and 646 nm) by MODerate Imaging Spectrometer (MODIS), in terms of ground-based Aerosol Robotic Network (AERONET) measurements of total column extinction aerosol optical depth (AOD, τ), and retrieved total column wavelength dependent SSA using radiative transfer calculations. Required information on aerosol particle size distribution is taken from an AERONET-based climatology specifically developed for this project. This inversion procedure is applied over 110 AERONET sites distributed worldwide, for which

20   continuous, long-term AERONET measurements are available. Using the derived data set we present seasonal and regional climatology of $\omega_o(\lambda)$ for carbonaceous, dust and urban/industrial aerosol types. The UV-Visible spectral dependence of ω_o obtained for the three major aerosol types from the synergy algorithm is found to be consistent with the insitu measurements reported in the literature. A comparison to standard AERONET SSA product at 646 nm shows absolute differences within 0.03 (0.05) for 40% (59%) of the compared observations.

25   The derived aerosol $\omega_o(\lambda)$ data set provides a valuable addition to the existing aerosol absorption record from AERONET by extending the absorption retrieval capability to the near-UV region. The combined UV-Visible data set, in addition to improving our understanding of spectral aerosol absorption properties, also offers wavelength-dependent dynamic aerosol absorption models for use in the satellite-based aerosol retrieval algorithms.

1 Introduction

Atmospheric aerosols play a significant role in the Earth's climate system through scattering and absorption of solar radiation, thus capable of perturbing radiation budget. The ratio of the amount of the light scattering to the total extinction referred to as single scattering albedo (SSA, ω_o) is a fundamental variable used to gauge the absorbing nature of aerosols. Mie-theory indicates ω_o equals to one for purely scattering aerosols and less than one towards zero for increasingly absorbing nature of aerosols. Studies show that the estimates of net aerosol radiative forcing is sensitive to the aerosol ω_o, and small changes to it could potentially alter the forcing on atmosphere (Chyacutelek and Coakley, 1974; Hansen et al., 1997). Models are often fed with essential aerosol properties to estimate the forcing on the atmosphere. These properties include aerosol optical depth (AOD, τ), complex refractive index, and phase function. Here, the knowledge on spectral dependence of such properties is crucial in quantifying the overall effects of aerosols. For example, absorbing aerosols can lead up to a 50% increase in the near-UV irradiance compared to the similar load of only scattering aerosols in the atmosphere (Bais et al., 2005). A report by Intergovernmental Panel on Climate Change suggests that the lack of spectral aerosol absorption is one of the major contributors leading to significant uncertainties in quantifying the net aerosol radiative effects on the Earth's climate (IPCC, 2013).

Developments in ground-based and satellite aerosol retrieval techniques have greatly improved our understanding of atmospheric aerosols over the last two decades. However, knowledge on spectral aerosol absorption properties is limited due to difficulties in measurements (e.g., Heintzenberg et al., 1997) and larger uncertainties in remote sensing retrievals (e.g,. Dubovik et al., 2000). Direct measurements of aerosol absorption can be obtained by using instruments that measure scattering and extinction coefficients. Such measurements are limited to discrete wavelengths and associated with few ground stations, laboratory measurements, or airborne field campaigns. Aerosol absorption can also be inferred from the sky radiance and extinction measurements that rely on fitting ground observations to radiative transfer calculations (Nakajima et al., 1996; Dubovik et al., 1998; Cattrall et al., 2003). Detailed reviews of measurements and techniques to retrieve aerosol absorption are available in several papers (e.g., Clarke et al., 1967; Bond and Bergstrom, 2006; Moosmüller et al., 2009). Among the ground-based sensors, currently, AERONET provides long-term aerosol absorption record at four discrete wavelengths from the visible (Vis) to near Infrared (NIR) spectrum over many sites distributed worldwide. The known limitation of AERONET absorption product is the lack of near-UV wavelengths, besides higher aerosol load ($\tau_{440} > 0.4$) and

high solar elevation angle required to obtain reliable absorption in Vis-NIR spectrum. These limitations make it

60 imperative to look for alternate data retrieval methods or sources to fill the knowledge gap.

For a few decades now, satellite remote sensing is used as an essential tool to gain a global perspective of aerosols distribution in the atmosphere. The satellite measured TOA reflectances are sensitive to both τ and ω_o, in addition to the surface reflectance. Most satellite aerosol retrieval techniques require making assumptions on

65 particle sizes (phase function) and ω_o to retrieve τ. On the other hand, several efforts have been made to estimate aerosol ω_o from direct satellite measurements at visible wavelengths (e.g., Kaufman, 1987; Kaufman et al., 2002; Satheesh and Srinivasan, 2005; Zhu et al., 2011) and near-UV wavelengths (Torres et al., 2007, 2013). However, the variety of natural surface types, choice of wavelengths, and aerosol models pose limitations on such techniques. In terms of wavelength, enhanced molecular scattering in the near-UV region acts as a strong

70 background and helps identify absorbing aerosols. However, to retrieve aerosol absorption using near-UV measurements, quantitative information on aerosol layer height (ALH) is required. The existing satellite aerosol retrieval techniques that rely on observations in the visible assume a constant ω_o value, and for a few sensors, it is still assumed wavelength-independent. A review on the commonly used satellite aerosol products singled out aerosol absorption as an inherent problem common to all sensors (Li et al., 2009). Studies using the evolving

75 ground-based aerosol record provides evidence that satellite retrieved τ can lead to large biases if the assumed aerosol ω_o is wavelength-independent (Jethva and Torres, 2011), and constant (Lyapustin et al., 2011; Eck et al., 2013). These studies highlight the importance of using wavelength-dependent aerosol ω_o and account for its spatial and temporal variability in the assumptions made for satellite retrieval of aerosol products.

80 In the past, few studies used both ground and satellite measurements to retrieve aerosol absorption properties. Li et al., (1999) used visible band radiances from AVHRR and in situ measured τ during SCAR-B experiment to derive absorption from biomass burning aerosols. Sinyuk et al., (2003) used UV-radiances from TOMS and aerosol extinction from AERONET to derive the imaginary refractive index of dust particles over a few stations in the Sahara belt region. Lee et al., (2007) estimated the aerosol SSA across a few stations over China using

85 combined ground and satellite (MODIS) measurements at visible wavelengths. Nonetheless, these studies are limited and do not provide a comprehensive characterization of absorbing aerosols from the UV-Visible spectrum.

The objectives of the present work are to derive columnar aerosol $\omega_o(\lambda)$, and its spectral dependence in the UV-Visible part of the spectrum. This approach makes use of the measured τ, and derived particle size distribution from AERONET in an inversion procedure. The A-train constellation of satellites that includes OMI and MODIS makes routine TOA measurements from the UV-Visible spectrum. Near-simultaneous measurements from A-train satellites provide an excellent opportunity to combine satellite and ground measurements during the overpass times (local noon, ~13:30 hrs) over the AERONET sites.

The organization of the remaining manuscript is as follows: section 2 describes the ground-based and satellite measurements used in this work. Section 3 describes the methodology adopted to derive aerosol $\omega_o(\lambda)$. Section 4 provides the sensitivity tests conducted to estimate the error incurred in the proposed aerosol absorption retrievals. Section 5 presents the seasonal variability in aerosol $\omega_o(\lambda)$ derived for sites distributed across major aerosol environments worldwide. Section 6 provides a discussion of the regional aerosol absorption models derived in this work. Section 7 presents a comparison of retrieved SSA with the AERONET absorption product. Finally, section 8 provides a summary of the work, along with the key findings and outlook for further studies.

2 Data sets

The details of ground-based and satellite data sets used in this work are provided in Table 1. Our usage of satellite data is strictly limited to the TOA reflectances, satellite-sun geometry, and other ancillary information (quality flags, aerosol type) but not the aerosol retrievals (τ) themselves from OMI and MODIS.

2.1 AERONET

Aerosol Robotic Network (AERONET) employs an automatic sun-tracking photometer to measure sun and sky radiances (Holben et al., 1998). The direct sun measurements are made at nine nominal wavelengths of 340, 380, 440, 500, 675, 870, 940, and 1020 nm typically for every 15 minutes interval. The extinction τ obtained from these measurements are accurate within ±0.01 (±0.02) at the visible (near-UV) wavelengths (Dubovik and King, 2000). In addition to the direct sun measurements, the photometer also measures multi-angular diffuse sky radiances along the almucantar plane at four distinct wavelengths from visible to the near-Infrared spectrum (440, 675, 870 and 1020 nm) with near-hourly frequency. An inversion procedure that uses both direct sun and angular sky radiances together is implemented to derive aerosol particle size distribution and complex refractive indices (Dubovik et al., 1998; Dubovik and King, 2000). The uncertainty in the derived spectral aerosol SSA provided by

the AERONET inversion Level 2 product is estimated to be ±0.03 for $\tau_{440} > 0.4$ (Dubovik et al., 2000). For the locations, where aerosol loading is usually low, the derived aerosol absorption properties have much higher retrieval error (Level 1.5 inversion product). In this work, we use AERONET measured columnar τ as a constraint to derive aerosol absorption from satellite TOA measurements. The particle size distributions provided by AERONET products are used for constructing a representative aerosol model for the associated sites. Aerosol absorption properties from AERONET Level 2 Version 3 product are used for comparison with our retrievals at visible wavelengths. Figure 1 shows the location of the total 110 AERONET sites used in this work for which long-term (> 7 years) quality assured Level 2 (version 3) measurements are available.

2.2 OMI

Launched in July 2004, the Ozone Monitoring Instrument (OMI) onboard NASA's EOS Aura satellite is a nadir-viewing hyper-spectral imaging radiometer (Levelt et al., 2006). OMI measures the TOA radiances in the wavelength range 270-500 nm with a ground pixel spatial resolution of 13 km x 24 km at nadir. OMI achieves daily global coverage in 14-15 orbits with a swath of 2600 km scanning the entire earth's surface. In this work, we use OMI radiances (340, 354, and 388 nm) provided in the in-house product OMLERWAVE and publicly accessible OMAERUV Level 2 aerosol product (V1.8.9.1). The OMLERWAVE product reports radiances and Lambertian equivalent reflectivity (LER) at several discrete wavelengths in the near-UV and visible parts of the spectrum. Additionally, we also use ancillary information on the quality of pixel (cloud contamination, land/sea mask, etc.), aerosol type, LER, and ALH data set used in the operational OMAERUV product. The OMAERUV product primarily relies on the measured near-UV aerosol index and AIRS-retrieved carbon monoxide information to categorize aerosols into Carbonaceous, Dust, and Urban/Industrial types. Since mid-2007, OMI suffers from an external obstruction that affects the quality of radiance measurements in a few rows (cross-track pixels). This is referred to as 'row anomaly' that restricts the current usage of OMI observations for the scientific purpose to about half in a total of 60 cross-track rows (Schenkeveld et al., 2017). Extensive documentation about how the row anomaly affects the OMAERUV aerosol product is available at Torres et al., (2018).

2.3 MODIS

The MODerate resolution Imaging Spectro-radiometer (MODIS) onboard NASA's EOS Aqua and Terra satellites are nadir-viewing, multi-spectral radiometer. MODIS measures the TOA radiances in 36 wavelength bands ranging from 0.41-14.23 μm with a ground pixel spatial resolution between 250-1000 m. MODIS scans the earth's surface with a 2300 km wide swath to provide near-global coverage on a daily basis. In this work, we use

Aqua-MODIS radiances (at 466 and 646 nm) provided in the 10-km aerosol product (MYD04_L2) from the Deep-Blue (DB) aerosol algorithm. This aerosol product provides cloud-free radiances and ancillary information on the quality of pixel and estimated cloud fraction.

3 Methodology

150   A schematic flowchart of the method adopted in this work to derive wavelength-dependent aerosol absorption is shown in Figure 2.

3.1 Computation of site-specific Look-up table of TOA reflectances

To start, we compile a seasonal climatology of aerosol particle size distributions and real part of the refractive index (440 nm) from the AERONET Level-2 Version-2 inversion product for each site considered in the study.
155   Here, we assume that the spectral variability of the real part of the aerosol refractive index through UV-Visible is minimal and, therefore, values derived at 440 nm were assumed to be wavelength-independent across the UV-Visible spectrum range considered in this study. The resulting climatology of aerosol size distribution are fed to a radiative transfer model (RTM) to generate look up table (LUT's) of outgoing top of the atmosphere (TOA) reflectances at 340, 354, 388, 466, and 646 nm with varying nodal points of satellite-sun geometry, surface
160   pressure, τ, ALH, and imaginary component of the refractive index. The Gauss-Seidel radiative transfer code (Mie theory) used for this purpose accounts for gaseous absorption, molecular and aerosol multiple scattering (Herman and Browning, 1965). Thus, a database of AERONET site-specific seasonal LUT of reflectances for the aerosols observed over each site in the study is created. Figure 3 shows the calculated net aerosol reflectance at the TOA over the GSFC site (38.92^{o} N, 76.84^{o} W) using particle sizes derived from the AERONET product and
165   varying values of τ and ω_o. These results illustrate that for a given satellite-sun geometry and observed radiance, multiple combinations of τ and ω_o can explain the satellite measurements. This simulation demonstrates that in order to derive ω_o from satellite measurements, an accurate characterization of τ, cloud-free radiances, and surface reflectances are required.

170   The site-specific LUTs developed here assume spherical particle shapes for carbonaceous and urban aerosols. However, mineral dust particles are assumed non-spherical and modeled as randomly oriented spheroid (Dubovik et al., 2006; Torres et al., 2018). To account for the non-spherical behavior of dust particles, a unified dust model is created using particle sizes from selected AERONET sites over Sahara and Arabian region that include: Saada,

SEDE_BOKER, Solar_Village, and Tamanrasset_INM. These sites were selected based on the observed
175   prevailing dust aerosol type. The particle sizes and real refractive index obtained at these sites are used with a
pre-computed set of kernels that assume a spheroidal shape with a fixed distribution of axis ratio to produce
phase function (Dubovik et al., 2006). The obtained phase matrix elements are input to the RTM to create
reflectance LUT's. The process of acquiring a unified dust model LUT is necessary to account for the non-
spheroidal shape of particles and save a considerable computational time, which otherwise would require to create
180   another set of site-specific LUTs.

3.2 Collocation of satellite and ground measurements

We use satellite measurements located within the 50 km radius of each AERONET site. In essence, we treat the
overlying atmospheric aerosols within a 50 km radius of the site as a representative of the AERONET measured
τ. To allow for more sampling, we associate the AERONET observations within ± 2 hours of satellite overpass to
185   the measured TOA radiances. Here, we do not employ any averaging scheme for the AERONET data and keep it
intact. While with satellite measurements, we use native pixel resolution of 13 km x 24 km for the OMI
wavelengths (340, 354 and 388 nm) and 10 km x 10 km resolution radiances for the MODIS wavelengths (466
and 646 nm).

3.3 Retrieval of aerosol $\omega_o(\lambda)$

190   The proposed technique to derive aerosol absorption follows the procedure of obtaining the best quality assured
cloud free-TOA reflectances, identifying the aerosol type, optimal layer height, and characterize surface
reflectance. We select over-land pixels from both sensors with the best quality flags ('0'-OMI, '3'-MODIS-DB)
and cloud fraction < 0.2 in the retrieval procedure. Aerosol type information for the OMI wavelengths is directly
adopted from the OMAERUV product. While for the MODIS wavelengths, our algorithm looks for the nearest
195   OMI footprint to obtain and assign the corresponding aerosol type. Once an absorbing aerosol type i.e.,
carbonaceous smoke or mineral dust is identified, we choose the best estimate of ALH from the joint OMI-
CALIOP climatology derived from a 30-month long record of collocated observations (Torres et al., 2013).
While for a weakly absorbing aerosol (Urban), ALH is characterized with a Gaussian distribution of aerosols
with a peak at the surface. This is similar to the procedure adopted in the OMAERUV aerosol retrieval (Torres et
200   al., 2013). For the surface characterization at OMI wavelengths, we use a near-UV surface albedo database used
in the OMAERUV algorithm. At MODIS wavelengths, surface reflectance provided by MAIAC products
(Lyapustin and Wang, 2018) is used. Our retrieval technique gathers all above-mentioned information for each

pixel along with the associated AERONET τ to perform an inversion for each wavelength independently. The inversion procedure solves for the best fit of radiances and τ with the prior computed site-specific seasonal LUT

205 radiances to derive aerosol $\omega_o(\lambda)$.

Figure 4 shows the retrieved aerosol SSA over the GSFC site as a function of measured τ. Located in the vicinity of a metro city, the prevailing aerosols over the GSFC site are the urban or industrial types that are relatively more scattering in nature. The mean aerosol SSA retrieved at the GSFC site for all τ observations at 340, 354,

210 388, 466 and 646 nm are 0.91, 0.93, 0.93, 0.90 and 0.85, respectively. The variability of the retrieved SSA is high at lower aerosol loading for all wavelengths. Particularly notable is the high variability of retrieved SSA in most τ bins for the visible wavelengths (i.e., MODIS bands). This is due to the weaker aerosol signal strength for urban type aerosols at lower aerosol loading in the visible spectrum, where the measured TOA radiances are dominantly contributed by the underlying surface. Also shown in figure 4 is the number of collocated observations that were

215 used in the inversion and the percent of observations for which SSA is retrieved. For about 12 years of the satellite and ground collocated observations used here, it is clearly evident that the number of observations from OMI is less than MODIS observations. The difference in the number of collocated observations stems partly from the OMI row-anomaly, cloud contamination, and the coarser pixel resolution. The percent of SSA retrieved observations varies widely even within the corresponding sensor wavelengths (OMI: 340, 354, 388 nm and

220 MODIS: 466, 646 nm). At times depending on the surface albedo used, the computed net aerosol reflectance might exceed the LUT limits and produce SSA values above one or less than the maximum absorption in the LUT. We avoid this by constraining our inversion procedure within the LUT limits and do not allow for any extrapolation of the inputs. However, this leads to the unequal number of retrieved observations within the sensor wavelengths. In other words, for a given observation within the OMI or MODIS sensor, it is possible to have

225 aerosol SSA retrieved at one wavelength and no retrieval (out-of-bounds) at other wavelengths. Also, it is worth mentioning that for few sites located along the coasts or in the islands (e.g., Mauna_Lao, Ascension_Island, Nauru), we were either unable to retrieve aerosol SSA or the number of days with retrieval is quite low. This is a consequence of OMI's large pixel size, where the satellite measured radiances are often contaminated by clouds and mixed-signal from the surface that are challenging to resolve and lead to out-of-bounds in the inversion.

230

To examine the seasonal variation of aerosol SSA and its spectral dependence, we create a subset of the data that includes observations for which aerosol SSA is retrieved for all the corresponding sensor wavelengths simultaneously (OMI: 340, 354, 388 nm and MODIS: 466, 646 nm) on any given day. This step reduces the

sample size drastically but eliminates the need for making prior assumptions on the wavelength dependence of
235   aerosol absorption angstrom exponent to fill those gaps. Instead, the obtained aerosol SSA in the UV-Visible
range is used to compute the resulting spectral dependence of aerosol absorption of the prevailing aerosols over
the corresponding AERONET sites in terms of the Aerosol Absorption Exponent (AAE), a measure of the
spectral dependence of aerosol absorption (Bond, 2001) using a power-law approximation, analogous to the
Angstrom Extinction Exponent (van de Hulst, 1957). The spectral dependence of aerosol absorption is reported
240   as Absorption Angstrom Exponent (AAE) defined as the slope of aerosol absorption optical depth with
wavelengths on a log-log scale. The aerosol absorption optical depth $\tau_{abs}(\lambda)$ is derived as shown in equation (1):

$$\tau_{abs}(\lambda) = \left(1 - \omega_0(\lambda)\right) . \tau_{ext}(\lambda) \tag{1}$$

from which the AAE for wavelength range λ_1, λ_2 is calculated as shown in equation (2).

$$AAE(\lambda_1, \lambda_2) = -\frac{\ln(\tau_{abs}(\lambda_1)/\tau_{abs}(\lambda_2))}{\ln(\lambda_1/\lambda_2)} \tag{2}$$

245   In addition, we make use of the AERONET extinction angstrom exponent (α) at 440-870 nm to distinguish the
particles as coarse (α < 0.2), fine (α > 1.2), and in between as intermediate or mixed-mode. Since our aerosol
identification strictly uses three primary types, the use of qualitative indicator α helps delineate the mixture of
aerosols when applicable.

4 SSA retrieval sensitivity analysis

250   The inversion procedure employed here to derive aerosol absorption from the combined ground and satellite
measurements is susceptible to several systematic and random errors. These error sources include: (a) aerosol
extinction measurements, (b) estimation of particle size distribution, (c) real part of refractive index, (d)
calibration of satellite measured TOA radiances, (e) surface reflectance, (f) aerosol layer height, and (g) sub-pixel
cloud contamination. The retrieved aerosol absorption from our inversion procedure could be affected by all these
255   sources of uncertainties. Among these, error sources from (a-d) are inevitable for which we do not have any
direct control over them. However, we do have control only for the sources from (e-g) in our retrieval. Errors
associated with surface reflectance, aerosol layer height, and cloud contaminations on the satellite retrieved
optical depths are well documented in the literature (e.g., Fraser and Kaufman, 1985; Torres et al., 1998; Jethva et
al., 2014). In summary it is known that an: (i) overestimation (underestimation) of surface reflectance leads to
260   lower (higher) aerosol SSA, (ii) overestimation (underestimation) of τ leads to lower (higher) aerosol SSA, (iii)
overestimation (underestimation) of ALH produces higher (lower) aerosol SSA – more pronounced in the UV
than in visible wavelengths, and (iv) an increase in TOA reflectance due to sub-pixel cloud contamination

produces higher aerosol SSA. We use sensitivity tests for these key input variables to derive a quantitative estimate of the error percolated in the aerosol SSA retrieval due to changes in these variables.

265

Sensitivity tests are performed on observations that were reported with best accuracy (minimal cloud contamination in both OMI and MODIS data sets) for a few selected sites that include GSFC, Avignon, Tamanrasset_INM, Saada, Alta_Floresta, and Mongu. These sites were selected to include different types of aerosols observed over these sites. Figure 5 shows the error analysis of the retrieved SSA as a function of

270 wavelength and optical depth given a change in the surface reflectance and ALH by an absolute change of ±0.01 and ±1 km ALH. The absolute error is computed as the SSA obtained with altered input minus the actual SSA. As expected, the error in retrieved SSA increases with increasing wavelength and decreasing τ due to changes in surface reflectance for all aerosol types. For less-absorbing (Urban) aerosols, the surface reflectance becomes increasingly important at the visible wavelengths than compared to absorbing aerosols. Our analysis shows that

275 for small τ_{440} (~0.2), the error in retrieved SSA is much higher (> ±0.05) for visible wavelengths, while that in the near-UV region reaches up to ±0.03. However, for observations with τ_{440} ~0.4, a reliable accuracy of within ±0.05 is achieved even for the non-absorbing aerosols at 646 nm. In contrast to the surface reflectivity, the effect of ALH becomes prominent at near-UV wavelengths. The error in retrieved SSA due to changes in ALH decreases with wavelength because of the gradually diminishing the intensity of Rayleigh scattering and its

280 radiative interactions with aerosols. The errors in the retrieved SSA are estimated to be better than ±0.03 in the near-UV and negligible at visible wavelengths for both absorbing and non-absorbing aerosols.

Table 2 presents the achievable accuracy in our SSA retrievals at 340 nm and 646 nm. Overall, for the observations with τ_{440} equals to 0.4, the estimated accuracy in our retrieved SSA is within ±0.03 (±0.05) for

285 absorbing (non-absorbing) aerosols through 340-646 nm. While for the observations with τ_{440} up to 0.2, the achievable accuracy in SSA reaches up to ±0.05 (> ±0.05) for absorbing (non-absorbing) aerosols.

5 Results

The results presented hereafter include only a data subset that meets the following three conditions: (a) SSA retrievals are available for all five wavelengths on a given day, (b) τ_{440} > 0.4, to ensure reliable accuracy spanning

290 through UV-Visible wavelengths, and (c) there are at least 5 days of observations available per season per aerosol type. We include results of retrieved SSA for cases when $\tau_{440} \leq 0.2$ as supplementary materials. Table 3 presents

seasonal averages of aerosol SSA and AAE for all sites considered in this work. The spectral dependence of absorption quantified as AAE is reported for three different wavelength pairs covering the near-UV (354, 388), Vis (466, 646) and UV-Vis (340, 646) spectra.

5.1 Biomass Burning

5.1.1 South America

The AERONET sites located in South America include Alta_Floresta, Arica, CEILAP-BA, CUIABA-Miranda, Rio_Branco, Ji_Parana_SE, SANTA_CRUZ_UTEPSA, Sao_Paulo and Campo_Grande_SONDA. In general, carbonaceous aerosols over South America are dominantly emitted from biomass burning during southern hemisphere spring (JJA) and summer (SON), with distinct peaks in August and September. Most aerosol emissions are associated with biomass burning for land and agricultural management practices. Further, densely populated places like Sao Paulo and CEILAP-BA are also affected by vehicular and industrial emissions. Aerosols from northern parts of the Amazon Basin advecting south or southeast, and long-range transport of aged smoke from Southern Africa are not uncommon over few locations in South America. Figure 6a shows regional average SSA for carbonaceous particles at 466 nm is noted to be 0.92 (0.93) during JJA (SON) months. Average τ_{440} and $\alpha_{440-870}$ are about 1 and 1.8 respectively for both seasons, indicating dominantly fine mode nature of these particles. Spectral SSA increases from 340 nm (0.90) to 388 nm (0.93) followed by a decrease toward the visible wavelengths. For urban aerosols, the average τ_{440} (0.57) and $\alpha_{440-870}$ (1.70) are lower than those of carbonaceous particles. The average SSA at 466 nm for urban aerosols is 0.88 (0.92) for JJA (SON) months. We also find that the urban aerosols in South America are more absorbing during JJA than in SON. Examining individual sites (Table 3) reveals high absorption during JJA at CUIABA and Sao Paulo. It is likely that the urban aerosol samples shown here attribute to a mixture of aerosols.

5.1.2 Southern Africa

The AERONET sites located in the Southern Africa are Mongu, Pretoria, and Skukuza. In addition to the natural forest fires and emissions from crop residue burning, heavy industrial facilities and episodic dust commonly dictate the aerosol amounts over Southern Africa. Figure 6b shows the regional average SSA derived for aerosols over the Southern Africa. For the carbonaceous and urban aerosols observed over the region, maximum absorption is found in JJA period. The average SSA for carbonaceous particles increases from 340 nm to 466 nm and then decreases at longer wavelengths. Distinct seasonality in absorption for carbonaceous particles is observed with maximum (minimum) value of 0.87 (0.90) at 466 nm for JJA (SON) months. The range of regional

average values of τ_{440} and $\alpha_{440\text{-}870}$ for carbonaceous particles are about 0.76 to 1.02 and 1.76 to 1.84 ranges respectively, while for urban aerosols the variability ranges are 0.55 to 0.73 and 1.68 to 1.74, respectively. As noted, τ_{440} and $\alpha_{440\text{-}870}$ are higher for carbonaceous particulate than for urban aerosols. For the latter, the average SSA shows similar spectral behavior as carbonaceous particles. However, the AAE of carbonaceous aerosols in

325 the UV-Vis range is noted to be ~1.73, while for urban aerosols it is ~2.2. Notable seasonality for urban aerosols is observed for DJF where the average SSA is almost flat from 340 nm to 466 nm with a slight increase thereafter. Aerosols organic components are likely the cause of such absorption spectral feature.

5.1.3 Australia

In general, inland Australia is categorized as arid-region vastly covered with deserts. However, Northern and
330 Western parts of the continent are covered with savanna grasslands, where biomass burning due to natural forest fires and land management practices are known to produce high aerosol emissions during the dry season (May-October). The regional average SSA for the aerosols observed over Northern Australia at the sites Jabiru and Lake_Argyle is shown in figure 6c. For the sample obtained in this work, carbonaceous and urban aerosols are found during spring (SON). The average τ_{440} and $\alpha_{440\text{-}870}$ for carbonaceous particles is 0.65 and 1.62, respectively.
335 Average SSA increases with wavelength from 0.87 (340 nm) to 0.89 (388 nm) and then decreases to 0.87 (646 nm). Such behavior of fine-mode particles is likely a result of a mixture of black carbon and organic carbon amounts in the atmosphere, producing stronger (weaker) absorption in the UV (Vis) wavelengths. Although the mean $\alpha_{440\text{-}870}$ for both carbonaceous and urban aerosols is similar, the mean τ_{440} for urban particles is relatively low. The UV-Vis spectral dependence of urban aerosols (1.57) follows similar behavior as carbonaceous aerosols
340 (1.42). Unlike the typical urban aerosol absorption, the spectral SSA observed here indicates a mixture of urban and carbonaceous particles.

5.2 Dust

5.2.1 Sahara

The seasonal average SSA of aerosols over the sites Saada and Tamanrasset is shown in figure 7a. As one would
345 expect from the region, dominantly dust aerosols are observed with average τ_{440} and $\alpha_{440\text{-}870}$ ranging from 0.63 to 0.85 and 0.11 to 0.16, respectively. Regional average aerosol SSA obtained at 466 nm is ~0.94. The spectral dependence of dust aerosols shows increase in SSA with wavelength, i.e., 0.86 at 340 nm to 0.97 at 646 nm. The UV-Vis AAE obtained for dust aerosols range from 2.8 to 3.3 with no distinct seasonality in the average spectral SSA. As noted, in addition to the coarse dust both sites constitute intermediate range of aerosols with average

350   $\alpha_{440-870}$ up to 0.3. Compared to coarse particles the intermediate sizes exhibit typical 'dust' absorption curve but has relatively low SSA (0.95) at 646 nm and therefore low UV-Vis AAE (2.1 to 2.5). This is consistent with the known dependence of scattering effects at longer wavelength for the dust particles.

5.2.2 Sahel

The AERONET sites located in the Sahel region are Agoufou, Banizoumbou, Dakar, IER_Cinzana, Ilorin,
355   Ouagauodu, and Zinder_Airport. Regional average SSA for the aerosols over Sahel region is shown in figure 7b. For dust aerosols, the average spectral SSA resembles typical dust absorption curve (increase in SSA with wavelength). No distinct seasonality in regional average absorption is observed. However, during SON months relatively low τ_{440} (0.64) and UV-Vis AAE (1.57) is noted compared to other seasons. Aerosols with intermediate size category ($0.2 < \alpha_{440-870} < 1.2$) are observed for all sites in the Sahel region. The spectral SSA obtained for
360   these aerosols clearly indicate mixture of dust and carbonaceous particles. Eck et al. (2003) reported smoke particles found toward southern parts of the West Africa are relatively coarse (α ranges 0.3 to 0.5) than those found elsewhere – likely a result of mixing with other aerosol types, coagulation, humidification or combination of such processes. Typical carbonaceous absorption curve noted here for the wet season (JJA and SON) is consistent with those reports. The average SSA for these (coarse-) carbonaceous particles is ~0.93 at 466 nm and
365   exhibit a UV-Vis AAE range 0.5 to 1.2. The average SSA observed for DJF and MAM (dry season) indicates a mixture of prevailing dust and carbonaceous particles. For the sample obtained over Sahel region, fine-mode carbonaceous and urban aerosols are observed at Ilorin during DJF and SON. Both these aerosol types show significant absorption with the average SSA at 340 nm and 646 nm is ~0.86 and 0.87, respectively, with nearly no spectral dependence. This likely indicates the presence of black carbon amounts over the Ilorin site during
370   DJF and SON. In addition to the biomass burning, fossil fuel combustion, and vehicular emissions, the vast number of gas flaring stations (> 300) around the Niger Delta produces high emissions (Onyeuwaoma et al., 2015). Highly absorbing black carbon amounts observed at Ilorin is possibly a result of such emissions.

5.2.3 Arabian Peninsula

The AERONET sites located in the Middle East/Arabian Peninsula region include Solar_Village,
375   SEDE_BOKER, Nes_Ziona, and Cairo_EMA_2. The regional average SSA of aerosols observed for these sites is shown in figure 7c. For dust aerosols, as expected, the average SSA increases with increasing wavelength. The regional average SSA ranges from 0.89 to 0.98 at 340 nm to 646 nm, with UV-Vis AAE in the range of 2.7 to 3.8. No distinct seasonality in SSA is found from our sample of observations. However, a slight increase in SSA

at UV wavelengths is noted during winter (DJF). Examining individual sites reveal this feature corresponds to the

380   aerosols over Solar_Village. The increase in SSA and high AAE_{354_388} noted for Solar_Village during DJF likely indicates transport of aerosols from neighboring regions. Intermediate range of particles with $0.2 < \alpha_{440-870} < 1.2$ are observed over all sites. The regional average SSA observed for these particles clearly indicate mixture of aerosols. Carbonaceous aerosols found over Cairo from our sample have average SSA ranging from 0.89 to 0.91 at 340 nm to 646 nm. The UV-Vis AAE (1.91) obtained for these aerosols likely indicate mixture of black and

385   organic carbon amounts. For the urban aerosols observed over Cairo and Nes Ziona the regional average SSA is found to be 0.89 at both 340 nm and 646 nm indicative of mixture of aerosols. While urban aerosols and pollution prevail over Nes Ziona, emissions from crop residue burning (rice straws) over the Nile delta region during winter (DJF) and heavy pollution dictate the aerosol absorption noted over Cairo.

5.3 Urban/Industrial

390   ### 5.3.1 Western North America

Dominantly urban type aerosols are observed in Western North America primarily produced from industrial activities and vehicle emissions. In addition, owing to the general meteorological and geographical setting of the western North America, the region experiences drier months in the summer and fall that initiates natural forest fires. The regional average aerosol SSA derived from our sample over the western North America is shown in

395   figure 8a. The average aerosol absorption for urban aerosols decreases in the wavelength range 340-388 nm followed by an increase at longer wavelengths. Carbonaceous aerosols are observed in our sample over the Missoula site located in the State of Montana. The average SSA retrieved for carbonaceous particles increases with wavelengths from 340 nm to 466 nm (0.89 at 0.94) and then decreases towards 646 nm (0.88). The average τ_{440}, $\alpha_{440-870}$ and UV-Vis AAE obtained for the carbonaceous particles are 1.74, 1.8 and 1.72 respectively.

400   ### 5.3.2 Eastern North America

Similar to the western part, atmospheric aerosols found over the eastern North America primarily originated from the industrial activities and secondary aerosol processes (Malm, 1992). Biomass burning generated carbonaceous particles and dust or mixture of aerosols over the eastern parts of the continent is a rare occurrence, except in the events of long-range transport of smoke from the west. Thus, the average aerosol SSA retrieved over the

405   AERONET sites in this region follows a typical 'Urban' spectral absorption curve, as shown in figure 8b. It is observed that aerosol SSA increases from the 340 nm to 388 nm or 466 nm and then decreases attaining a maximum absorption (~0.90) at 646 nm. The regional average SSA for the MAM and JJA months at 466 nm is

0.89 and 0.87 respectively. It should be noted that for urban aerosols the retrieval error at visible wavelength is high (up to 0.05). Since there are no notable changes in the aerosol sources, the observed decrease absorption at

410   646 nm for JJA period is likely attributed from the retrieval uncertainty.

5.3.3 Europe

For the AERONET sites located in the Europe, dominantly urban aerosols are observed (figure 8c). The regional average SSA increases from 340 nm to 388 nm and then decreases reaching a minimum value (0.83) at 646 nm for most seasons. The observed aerosol absorption is similar for spring (MAM) and summer (JJA). However,

415   there is an increase in absorption at wavelengths other than 646 nm for fall (SON) that reaches a maximum absorption 0.86 and 0.89 at 340 nm and 466 nm respectively. This likely suggests the presence of organic carbon amounts emitted from local fuel combustion sources. This feature is consistent with Ilias et al., (2019), that reports annual cycle of aerosol absorption over Thessaloniki site. Individual site observations reveal this increase in absorption is prominent for most locations in Europe during fall (Table 3) and winter (Table S1). While the

420   aerosol loading is similar throughout the seasons, the average UV-Vis AAE for urban aerosols range from 1.0 to 1.26. In addition to the urban/industrial aerosols, long-range transport of dust from Sahara is not uncommon over central Europe and Mediterranean Basin. Although our sample over European sites do not constitute any coarse mode particles, intermediate range ($0.2 < \alpha_{440\text{-}870} < 1.2$) of aerosols are observed for most sites. The average SSA curve noted here indicates mixture of aerosols.

425   ## 5.4 Mixed aerosol types

5.4.1 Mid-Atlantic North America

The seasonal average aerosol SSA obtained over the Mexico City is shown in figure 9a. Unlike typical urban aerosol absorption, the SSA curve obtained here shows steep decrease from 388 nm to 466 nm and remains flat or slightly decreases till the 646 nm. Seasonality in aerosol absorption is observed at UV wavelengths (< 400 nm)

430   with maximum (DJF, SON) and minimum (MAM) absorption of 0.86 and 0.91 at 354 nm. It is clearly evident that such absorption curve and seasonal variation is a result of prevailing mixture of aerosols. Seasonal average $\alpha_{440\text{-}870}$ indicates the prevalence of fine mode particles over the Mexico City. The average SSA at 466 nm for DJF, MAM and SON months are 0.85, 0.86 and 0.84 respectively. Although the seasonal average UV-Vis AAE of aerosols over Mexico City ranges from 0.94-1.27, the AAE_{354_388} is higher for (5.13) MAM than compared to

435   (2.2) DJF and (0.6) SON months. In general, Mexico City is a densely populated urban location that is well known for its high pollution levels among the other megacities worldwide. In addition to the high concentration

of aerosols from fossil fuel combustion throughout the year, Mexico City also experiences biomass-burning aerosols during the relatively dry months of March-May from local sources (Eck et al., 1998).

5.4.2 North-Eastern Asia

440 The AERONET sites located in the Northeastern Asia include: Beijing, Osaka, Shirahama and XiangHe. Figure 9b shows the regional average SSA derived over Northeastern China. For the samples obtained, dust aerosols possibly mixed with regional pollution are observed over Beijing and XiangHe during spring (MAM). The spectral curve of regional average SSA shows an increase from 0.87 at 340 nm to 0.95 at 646 nm. The UV-Vis AAE obtained for the dust aerosols is 1.56. Among sites considered here, carbonaceous aerosols are observed

445 throughout the year at Beijing and XiangHe. The spectral behavior of carbonaceous aerosols shows increase in SSA from 340 nm to 466 nm and thereafter remains near constant or slightly decreases with an UV-Vis dependence ranging from 1.84 to 2.14. However, significant seasonality is noted with minimum (0.95 at 466 nm) and maximum (0.90 at 466 nm) absorption during JJA and DJF respectively. The increase in SSA likely caused the humidification and secondary aerosol processes during JJA. Carbonaceous and urban aerosols over the region

450 show high absorption in winter (DJF), likely due to high amounts of local fossil fuel combustion and agricultural waste burning. The spectral behavior of urban aerosols is similar to carbonaceous aerosols with decrease in magnitude of average SSA, AOD, and UV-Vis AAE. As expected from the local sources, mixture of aerosols categorized by particle sizes ($0.2 < \alpha_{440-870} < 1.2$) is observed at all sites in the region with widely varying spectral dependence.

455 **5.4.3 Northern India**

The AERONET sites located in Northern India include Jaipur, Gandhi College and Kanpur. Major source of aerosols over the region includes industrial and vehicular emissions, combustion of biomass and fossil fuels. In addition, desert dust passage from arid and semiarid regions of northwestern India, Pakistan, and Arabian Peninsula is commonly observed during spring and summer months. Figure 9c shows the regional average

460 aerosol absorption observed at Kanpur. As expected from the source regions, dust aerosols are observed during spring (MAM) and summer (JJA) months over Jaipur and Kanpur. The average SSA shows a steep increase from 340 nm (0.88) to 466 nm (0.95), and a relatively smaller increase from 466 nm to 646 nm (0.97). The dust aerosols noted here has average τ_{440} 0.73 to 0.77 and exhibit UV-Vis AAE between from 2.9 to 3.4. For our sample, carbonaceous aerosols are observed over Kanpur and Gandhi College with similar regional average

465 absorption during SON and DJF. The spectral behavior of carbonaceous aerosols shows increase in average SSA

from 340 nm (0.91) to 466 nm (0.93) and slight decrease till 646 nm (0.91). The regional average UV-Vis AAE for carbonaceous aerosols range 1.2 to 1.5. Emissions from crop residue burning during SON and biomass burning for residential heating in DJF prevail over the entire Indo-Gangetic plain and likely result in such absorption. In addition the vehicular and industrial emissions add an extra burden of aerosols to the atmosphere.

470 In other words, urban aerosols over the Northern India can be categorized as carbonaceous aerosols resulting from various carbon emitting, both black and organic carbon, sources such as crop residue burning, local biomass burning for house-hold heating purposes in DJF months, vehicular and industrial emissions. These urban aerosols are relatively more absorbing (ω_o(466) ~0.89) than the carbonaceous aerosols (ω_o(466) ~0.93) from industrial/vehicular activities observed over Northern India. Throughout the seasons, influence of pollution

475 aerosols is clearly evident in the observed urban aerosol absorption. Although the UV-Vis AAE is found to be in the similar range, the AAE_{354_388} values are low for urban than carbonaceous aerosols indicative of high organic amounts in crop-residue/biomass burning emissions. For the group of aerosols in between the fine and coarse mode the spectral variation of SSA varies widely.

6 Discussion

480 Through extensive studies in the literature it is known that optical properties of biomass burning aerosols depend on fuel/vegetation type, combustion processes, available moisture content (e.g., Ward, 1992; Reid and Hobbs, 1998; Reid et al., 1998; Eck et al., 2001). Such studies reported varying properties of aerosols emitted from two phases of vegetation burning: flaming and smoldering. While flaming phase rapidly oxidizes the available volatile hydrocarbons in the biomass, smoldering phase mostly requires a surface where slow diffuse oxygen

485 converts the biomass through exothermic reaction. In general, burning of grasslands happens through flaming combustion process that emits high amounts of soot, while smoldering combustion prevail the burning of woodlands/deciduous forest that emits less soot. The observed aerosol absorption at the biomass burning sites (figure 6) clearly makes this distinction. Over South America, in addition to the emissions from burning rainforest (near by Alta Floresta and Ji Parana), Cerrado (wooded grasslands) type vegetation dominates at most

490 sites considered here. Such biomass burning occurs through smoldering combustion exhibiting relatively high aerosol ω_o (0.93 at 466 nm). Compared to South America, the aerosols over Southern Africa have distinct seasonality and high absorption (figure 6b). Eck et al (2013) demonstrated that this seasonality in aerosol absorption is likely a result of shift in fuel type and combustion process. At the beginning of dry season (starting June), the central region is prone to undergo a rapid burning through flaming process, while in the late dry season

495 (ends November) the wooded lands located southeastern parts begins to burn through dominantly smoldering process. For the savanna with open grasslands in the northern Australia, biomass burning happens through flaming combustion producing high amounts of soot, as also noted in our retrievals. Figure 10 shows the regional average AAE obtained for carbonaceous aerosols at three wavelength pairs. Overall, the average slope of absorption in visible (AAE_{466_646}) and UV-Vis (AAE_{340_646}) for carbonaceous aerosols is found to be within 2.

500 This is consistent with the studies that report AAE of biomass burning aerosols from several field campaigns in the range 1 to 3 (Kirchstetter et al., 2004; Schnaiter et al., 2005; Bergstrom et al., 2007; Clarke et al., 2007). However, the average AAE_{354_388} obtained is high up to 4 for most regions. This is likely a result of higher organic matter in the regional biomass types and highlights the importance of UV spectral region in delineating such group of aerosols. For the savanna grasslands in Australia where flaming combustion prevails the mean

505 AAE_{354_388} is relatively low (2.2 or less) compared to other biomass burning regions. For the sample obtained at Ilorin in Sahel and Cairo in the Arabian Peninsula, the mean AAE was found up to 2 for all wavelength pairs. Further, it is noted that carbonaceous aerosols observed over Northern India, Northeastern China, Sahel, and Arabian Peninsula has an average $\alpha_{440-870}$ ~1.4 (i.e, at the lower end of the fine-mode range), while in South America, South Africa and Australia has average ~1.8. This indicates the role of aerosol mixing and secondary

510 processes in emanating the observed variability in aerosol absorption other than its composition alone.

For dust aerosols, minerals such as hematite and other form of oxides play role in scattering/absorption of particles. The absorbing nature of pure dust aerosols close to the source is sensitive to the presence of hematite than other minerals at shorter wavelengths (Sokolik and Toon, 1999). In addition to the sedimentation of coarse

515 aggregates, the dust aerosols observed away from the source are often found to have mixed (internally or externally) with anthropogenic aerosols altering its absorbing nature. For example, ω_o of dust aerosols were reported as 0.83 to 0.87 near the source and ~0.9 far away from the source over the tropical North Atlantic Ocean using satellite measurements at 331 nm (Torres et al., 2002). For the dust aerosol samples obtained in this work, high absorption at 340 nm with a regional average of ~0.86 is noted for Sahara, while relatively lower absorption

520 ~0.90 is noted for the Sahel region. The mixing of dust with biomass burning emissions and local pollutants over the Sahel likely attributed to the observed low absorption. Similar low absorption (0.90) of dust at 340 nm is observed for the Arabian Peninsula region. However, the UV-Vis spectral dependence noted at the Sahel, and Arabian Peninsula varies significantly. Figure 11 shows the regional average AAE obtained for dust aerosols at three-wavelength pairs. Among the dust-prone regions considered here, the regional average of the UV-Vis

525 spectral dependence (AAE_{340_646}) is found to be close to or greater than 3 for all, except the Sahel and Eastern

China, where average value ranges 1.5 to 2.5. Although no distinct seasonal variation in spectral absorption of dust is noted, the variability in spectral dependence over the regions is quite evident. Overall the regional average of AAE for dust aerosols observed here is consistent with insitu measurements that report values ranging 1.5 to 3.5 (Bergstrom et al., 2004, 2007; Müller et al., 2009; Petzold et al., 2009). However, observations at individual

530   sites (Table 3) show that the spectral dependence of the observed dust for few sites is relatively high than those reported by insitu measurements. Considering our retrieval method where aerosol absorption is derived independently for each wavelength and have computed the dependence, our results agree reasonably well with the insitu measurements reported in the literature.

535   While urban aerosols constitute dominantly sulfates and other forms of nitrate particles, industrial emissions and fossil fuel combustion produces various forms of carbon that contribute to the overall optical properties. Further the aerosol size growth due to increase in relative humidity in the atmosphere and coagulation processes are known to alter the absorbing nature of aerosols. Figure 12 shows the regional average AAE obtained for urban aerosols at three-wavelength pairs. Urban aerosols in highly polluted environments such as over the Mexico City

540   have near unity spectral dependence. While the passage of biomass burning emissions over such environment show unusual decrease in absorption at the UV region attributing to high AAE_{354_388}. This is consistent with studies that report relatively high AAE in UV region and near unity in visible region for the aerosol mixture consisting of organic matter and black carbon amounts (Barnard et al., 2008; Vanderlei Martins et al., 2009; Bergstrom et al., 2010; Jethva and Torres, 2011). The urban aerosols found in our sample over Northern Indian

545   and Eastern China are highly absorbing exhibiting AAE_{340_646} ~1.5 than the carbonaceous aerosols with AAE_{340_646} ~2. These results suggest the combination of magnitude of aerosol absorption and its spectral dependence in UV, visible and UV-Visible spectrum could be used to partition mixture of aerosol types found in such environments. Overall the regional average UV-Visible AAE for the urban aerosols is found to be near 2.

7 Comparison with AERONET SSA product

550   We compare of our aerosol SSA retrievals at the visible wavelengths with that available from AERONET data set. The comparison of SSA retrievals is limited to $\tau_{440} > 0.4$ and where AERONET Level-2 inversion is available. It should be noted that since AERONET SSA is a derived quantity and cannot be considered as 'ground truth', this comparison serves as a consistency check rather than a validation exercise. For ease in comparison, we transform the AERONET SSA at 440 and 675 nm to MODIS wavelengths of 466 and 646 nm

555 respectively following interpolation. This conversion will unlikely introduce any bias in our comparison as the
difference in the nearest wavelengths of both data sets is very low (< 30 nm).

First, we investigate the consistency of retrieved SSA for selected sites for which the prevailing aerosol types and
local source environment are well known as documented in several studies in the literature. We use the
560 AERONET SSA from time period 2005-2016 for the comparison. Figure 13 shows the comparison of average
spectral SSA for three distinct aerosol types sampled from the selected sites. The vertical bars shown in the figure
corresponds to the uncertainty estimate provided by AERONET (±0.03) and the estimate due to change in ±0.01
surface reflectance for our retrieved SSA (±0.05). For dust aerosols, the retrieved average SSA show good
agreement with AERONET SSA obtained at Dakar and Ouagadougou (within ±0.008), while the differences in
565 SSA (retrieved minus AERONET) at Tamanrasset and Solar Village are +0.02 and +0.05 respectively at 466 nm.
Although our sample is limited for few days that met our criteria for subset, the observed differences in SSA are
within the uncertainty estimates as also noted from the overlapping error bars. For carbonaceous particles, the
retrieved and AERONET SSA agree well with differences of less than 0.015 for Alta_Floresta, CUIABA and
Mongu. However, notable difference in SSA (0.045) is observed at the Lake_Argyle with high absorption for
570 AERONET than our retrieved value at both 466 nm and 646 nm. It should be noted that, while AERONET
version 3 employs surface reflectance following BRDF parameters from MODIS BRDF/Albedo CMG Gap-Filled
Snow-Free Product MCD43GF (Sinyuk et al., 2020), we use MODIS MCD19A1 surface reflectance product. For
absorbing aerosols, the SSA differences observed here is likely a result of different surface reflectances data
employed by the two data sets. For urban/industrial aerosols at GSFC, Avignon, Moldova and Cairo the retrieved
575 SSA agrees within the uncertainty estimates. Particularly notable difference (–0.05) is found for Avignon at 646
nm.

Figure 14 shows the comparison of retrieved SSA with AERONET for all collocated observations. For the SSA
at 466 nm, the observations within ±0.03 (±0.05) envelopes are 26% (59%), 38% (63%) and 34% (56%) for dust,
580 carbonaceous, and urban aerosol types, respectively. It is observed that for dust aerosols, the observations are
well concentrated in a narrow range of SSA (retrieved values range from 0.92 to 0.99 at 466 nm), while for
carbonaceous (0.86 to 0.95 at 466nm) and urban types (0.84 to 0.98 at 466 nm) the observations become
increasingly scattered through wide range of SSA. In terms of wavelength, the observations at 646 nm are more
widely scattered than for the SSA at 466 nm for all aerosol types. For the SSA at 646 nm, the observations within
585 ±0.03 (±0.05) envelopes are 73% (87%), 39% (60%) and 28% (45%) for dust, carbonaceous, and urban aerosol

types, respectively. The root mean square error (RMSE) of the SSA ranges from 0.04 to 0.09 with lowest error for dust particles at 646 nm and highest error for urban aerosols at 646 nm. Among the aerosol types, it is noted that our retrieved SSA for dust at 466 nm has relatively high scattering than AERONET, while for other types the results are found to be consistent.

590

Figure 15a shows the comparison of retrieved SSA with AERONET by combining all aerosol types together. Our retrieved SSA at 466 and 646 nm agree with AERONET SSA for 34% (0.06) and 40% (0.07) of observations (RMSE) respectively. The absolute difference in retrieved and AERONET SSA as a function of optical depth is shown in figure 15b. The differences in SSA for both wavelengths at 466 nm and 646 nm are higher for lower τ

595 and become negligible for higher τ. It is observed that at 466 nm, the observations with positive differences are relatively more than that at 646 nm. It is important to note here that our retrieval method and that used in the AERONET inversion differ fundamentally in several aspects. Other than the different source of surface reflectance data used, one major distinction between the two methods is that the present inversion algorithm retrieves SSA at different UV and Vis wavelengths independently, whereas the AERONET algorithm internally

600 applies a condition ensuring the spectral shape of SSA follows an expected pattern for the observed aerosol type (private communication with Thomas Eck, NASA GSFC). The differences noted between our SSA retrievals and that from AERONET at different wavelengths could be attributed, at least partially, to this treatment of reported values of SSA.

8 Summary

605 Ground-based measurements of direct solar radiation under cloud-free conditions over worldwide sites are providing valuable insights into regional aerosol characteristics. Long-term measurements obtained from such network, such as from AERONET, are widely used to develop regional aerosol climatology and investigate seasonal/annual variability. Satellite measurements of TOA radiances are able to provide global distribution of columnar aerosol amounts. However, deriving aerosol optical properties from satellite measurements require

610 constraints on particle sizes and optical properties. Reliable aerosol measurements from ground-networks and airborne/field campaigns are traditionally used to validate and improve the constraints in satellite aerosol retrievals. In this work, we use AERONET measured extinction τ as constraint in a robust inversion technique that uses satellite measured TOA radiances from OMI and MODIS to derive spectral aerosol absorption in the UV-Vis part of the spectrum. Other than cloud contamination of the TOA radiances, major sources of error in our

615   retrieved SSA come from surface reflectance, and aerosol layer height. We use TOA radiance observations with
minimal or no cloud-contamination reported by both OMI and MODIS products. Sensitivity tests show that our
retrieved aerosol SSA has reliable accuracy up to ±0.03 from UV-Visible wavelengths for absorbing aerosols
(carbonaceous and dust) with τ_{440} > 0.4. However for less-absorbing aerosols the error in SSA retrieval reaches
up to ±0.05. For the sites with low aerosol loading (i.e, τ_{440} up to 0.2) the accuracy of retrieved SSA reaches up to

620   ±0.05 at the UV wavelengths, while in the visible it exceeds ±0.05. Using a subset of results where SSA is
retrieved independently for 340, 354, 388, 466 and 646 nm wavelengths for the same day with observations τ_{440} >
0.4, we examine the seasonal variability in aerosol SSA and derive spectral dependence (AAE) at three
wavelength pairs in the UV-Vis spectrum.

625   Key observations noted from the spectral aerosol absorption data set derived here are highlighted below:

Biomass burning aerosols

   a)   Among sites dominated by biomass burning aerosols, Mongu in Southern Africa has high absorption ω_o
        ~0.85 to 0.84 from 340 nm to 646 nm.

   b)   Strong seasonality in absorption of carbonaceous aerosols is evident in Southern Africa indicating the

630   role of biomass types and combustion process. The average ω_o from 340 nm to 646 nm during JJA and
        SON are ~0.85 to 0.84, and ~0.88 to 0.89, respectively.

   c)   Carbonaceous aerosols found over Northern Australia are as strongly absorbing (ω_o ~0.87 to 0.86 from
        340 nm to 646 nm) as smoke over Southern Africa but has relatively constant absorption from UV-Vis
        spectra.

635   d)   Carbonaceous aerosols found over Alta_Floresta in the Amazon Basin have similar absorption (ω_o ~0.89
        to 0.91 from 340 nm to 646 nm) and UV-Vis AAE (1.8) to those found over Missoula in North America.

   e)   Highly absorbing carbonaceous aerosols (ω_o ~0.86 to 0.87 from 340 nm to 646 nm) with weak spectral
        dependence are found in Cairo and Ilorin in the Sahel region during winter (DJF). These carbonaceous
        particles exhibit mean $\alpha_{440-870}$ < 1.4, indicating possible mixture of fine and coarse modes.

640   f)   Carbonaceous aerosols found over Northern India, Eastern China, Sahel, and Arabian Peninsula
        exhibiting (ω_o ~0.86 to 0.89 at 340 nm) has low average $\alpha_{440-870}$ (< 1.4) than over other prominent
        biomass burning regions, suggesting mixture of fine and coarse modes.

   g)   Distinct seasonality in spectral absorption of carbonaceous and urban aerosols is noted for Eastern China.
        For carbonaceous aerosols, the maximum and minimum absorption at 466 nm are found during DJF

645   ~0.90, and JJA ~0.95, respectively.

Dust aerosols

   a) For desert dust aerosols, the SSA is known to increase with wavelength from UV to Visible spectrum. No distinct seasonality in SSA is noted. The regional averages of SSA for dust aerosols from 340 nm to 646 nm are 0.86 to 0.98, 0.88 to 0.96, and 0.90 to 0.99 over Sahara, Sahel and Arabian Peninsula respectively.

   b) For regions where sources are nearby the sites (Sahara, Middle East/Arabian Peninsula) the AAE for all three wavelength pairs considered exhibit high average values (>> 3), while for regions where lofted dust through long-range transport is observed (Northern India, Eastern China, parts of Sahel) the average AAE has a range between 2 to 3.

Urban aerosols

   a) Urban aerosols ($\omega_o(340)$ ~0.87) are more absorbing than the carbonaceous aerosols ($\omega_o(340)$ ~0.90) and exhibit distinct seasonality (higher absorption during JJA than SON) in South America at CUIABA and Sao Paulo. The urban aerosols noted here are likely mixtures of carbonaceous particles transported over the region and prevailing pollution from local sources.

   b) High absorption from UV ($\omega_o(340)$ ~0.87) extending to the blue spectral region ($\omega_o(466)$ ~0.90) is noted for most sites in Europe during SON and/or DJF months indicating the presence of organic matter due to local fuel combustion sources.

   c) Polluted aerosols observed over Mexico City shows high absorption in UV ($\omega_o(340)$ ~0.88) extending to visible ($\omega_o(466)$ ~0.85) spectrum during DJF and SON months.

As mentioned, the results presented here are limited to our subset of retrievals, where SSA is retrieved for all five wavelengths from UV-Visible range with $\tau_{440} > 0.4$. However, relaxing the τ_{440} up to 0.2 (see supplementary materials) does not yield significant changes in the derived variability of aerosol absorption and its spectral dependence. Since one of our objectives is to derive UV-Visible spectral dependence (AAE) of aerosols without prior assumptions, and given the inherent sampling bias of the OMI, MODIS and AERONET colocations – the analysis method employed here is well justified. In other words, we made use of the best available data synergy and derive unique aerosol absorption data set with no prior assumptions on wavelength dependence, which otherwise is assumed in the standard satellite-based aerosol retrieval algorithm. Although our results may be

biased toward dense pollution/industrial, smoke, and dust events, less-absorbing low aerosol amounts seldom have dependency on the ω_o. Therefore, the regional aerosol absorption models derived here offer essential guidance for selecting spectral absorption in satellite aerosol retrievals spanning the UV-Vis spectrum. From our

680   analysis of worldwide inland sites: (a) it is suggested that satellite aerosol retrieval techniques could employ regional dynamic absorption models to avoid potential bias in τ retrievals noted in earlier studies, and (b) the spectral dependence of aerosol absorption noted here for the UV (354-388 nm), visible (466-646 nm) and UV-Visible (340-646 nm) range for all aerosol types other than black carbon varies considerably. Overall, the UV absorption data set well compliments and provides more information on the regional aerosol absorption than with

685   the visible data set alone.

Given the lack of aerosol absorption information at near-UV wavelengths in the existing AERONET record and limited availability of insitu measurements, the UV-Vis aerosol absorption data set developed here, perhaps for the first time, offers a valuable source of information useful for a variety of aerosol and trace gas studies. The

690   analysis presented here focuses on regional aerosol absorption using a subset of results. The derived spectral dependency can be used with all SSA retrievals to construct and investigate long-term trends in UV-Visible aerosol absorption. Further, the spectral aerosol SSA derived here could be used to parameterize absorption in models and better understand the radiative effect of aerosols. Our ongoing investigation utilizing the complete data set developed here will explore some of these applications in the future.

695   **Acknowledgments**

NASA ROSES (ACMAP) – 2016 provided financial support for this work under the grant NNH16ZDA001N. The authors are grateful to Brent Holben and the entire AERONET team for their efforts on maintaining AERONET sites worldwide and providing quality assured data to the community. The authors thank all PIs and Co-PIs of the individual AERONET sites that were used in this work.

700   **Competing Interests**

The authors declare no conflict of interests.

Author Contributions

Omar Torres (OT) and Hiren Jethva (HJ) had conceptualized the research. Vinay Kayetha (VK) developed the data set, performed formal analysis, and wrote the manuscript with inputs from OT and HJ. All authors reviewed

705   results, helped with the data interpretation and edited the manuscript to make a final version.

Data Availability

The spectral aerosol absorption data set developed here will be made available upon request to the authors.

References

710 Bais, A. F., Kazantzidis, A., Kazadzis, S., Balis, D. S., Zerefos, C. S. and Meleti, C.: Deriving an effective aerosol single scattering albedo from spectral surface UV irradiance measurements, Atmos. Environ., 39(6), 1093–1102, doi:10.1016/j.atmosenv.2004.09.080, 2005.

Barnard, J. C., Volkamer, R. and Kassianov, E. I.: Estimation of the mass absorption cross section of the organic
715 carbon component of aerosols in the Mexico City metropolitan area, Atmos. Chem. Phys., 8(22), 6665–6679, doi:10.5194/acp-8-6665-2008, 2008.

Bergstrom, R. W., Pilewskie, P., Pommier, J., Rabbette, M., Russell, P. B., Schmid, B., Redemann, J., Higurashi, A., Nakajima, T. and Quinn, P. K.: Spectral absorption of solar radiation by aerosols during ACE-Asia, J.
720 Geophys. Res. D Atmos., 109(D19), 1–13, doi:10.1029/2003JD004467, 2004.

Bergstrom, R. W., Pilewskie, P., Russell, P. B., Redemann, J., Bond, T. C., Quinn, P. K. and Sierau, B.: Spectral absorption properties of atmospheric aerosols, Atmos. Chem. Phys., 7(23), 5937–5943, doi:10.5194/acp-7-5937-2007, 2007.
725
Bergstrom, R. W., Schmidt, K. S., Coddington, O., Pilewskie, P., Guan, H., Livingston, J. M., Redemann, J. and Russell, P. B.: Aerosol spectral absorption in the Mexico City area: Results from airborne measurements during MILAGRO/INTEX B, Atmos. Chem. Phys., 10(13), 6333–6343, doi:10.5194/acp-10-6333-2010, 2010.

730 Bond, T. C.: Spectral dependence of visible light absorption by carbonaceous particles emitted from coal combustion, Geophys. Res. Lett., 28(21), 4075–4078, doi:10.1029/2001GL013652, 2001.

Bond, T. C. and Bergstrom, R. W.: Light absorption by carbonaceous particles: An investigative review, Aerosol Sci. Technol., 40(1), 27–67, doi:10.1080/02786820500421521, 2006.
735
Cattrall, C., Carder, K. L. and Gordon, H. R.: Columnar aerosol single-scattering albedo and phase function retrieved from sky radiance over the ocean: Measurements of Saharan dust, J. Geophys. Res. Atmos., 108(D9), 1–10, doi:10.1029/2002jd002497, 2003.

740 Chyacutelek, P. and Coakley, J. A.: Aerosols and Climate, Science., 183(4120), 75–77, doi:10.1126/science.183.4120.75, 1974.

Clarke, A., McNaughton, C., Kapustin, V., Shinozuka, Y., Howell, S., Dibb, J., Zhou, J., Anderson, B. E., Brekhovskikh, V., Turner, H. and Pinkerton, M.: Biomass burning and pollution aerosol over North America:
745 Organic components and their influence on spectral optical properties and humidification response, J. Geophys. Res. Atmos., 112(D12), 1–13, doi:10.1029/2006JD007777, 2007.

Clarke, A. D., Noone, K. J., Heintzenberg, J., Warren, S. G. and Covert, D. S.: Aerosol light absorption measurement techniques: Analysis and intercomparisons, Atmos. Environ., 21(6), 1455–1465, doi:10.1016/0004-
750 6981(67)90093-5, 1967.

Dubovik, O. and King, M. D.: A flexible inversion algorithm for retrieval of aerosol optical properties from Sun and sky radiance measurements, J. Geophys. Res. Atmos., doi:10.1029/2000JD900282, 2000.

755 Dubovik, O., Holben, B. N., Kaufman, Y. J., Yamasoe, M., Smimov, A., Tanré, D. and Slutsker, I.: Single-scattering albedo of smoke retrieved from the sky radiance and solar transmittance measured from ground, J. Geophys. Res. Atmos., 103(D24), 31903–31923, doi:10.1029/98JD02276, 1998.

Dubovik, O., Smirnov, A., Holben, B. N., King, M. D., Kaufman, Y. J., Eck, T. F. and Slutsker, I.: Accuracy
760 assessments of aerosol optical properties retrieved from Aerosol Robotic Network (AERONET) Sun and sky radiance measurements, J. Geophys. Res. Atmos., 105(D8), 9791–9806, doi:10.1029/2000JD900040, 2000.

Dubovik, O., Sinyuk, A., Lapyonok, T., Holben, B. N., Mishchenko, M., Yang, P., Eck, T. F., Volten, H., Muñoz, O., Veihelmann, B., van der Zande, W. J., Leon, J. F., Sorokin, M. and Slutsker, I.: Application of spheroid
765 models to account for aerosol particle nonsphericity in remote sensing of desert dust, J. Geophys. Res. Atmos., 111(D11208), 1–34, doi:10.1029/2005JD006619, 2006.
Eck, T. F., Holben, B. N., Slutsker, I. and Setzer, A.: Measurements of irradiance attenuation and estimation of aerosol single scattering albedo for biomass burning aerosols in Amazonia, J. Geophys. Res. Atmos., doi:10.1029/98JD00399, 1998.
770
Eck, T. F., Holben, B. N., Ward, D. E., Dubovik, O., Reid, J. S., Smirnov, A., Mukelabai, M. M., Hsu, N. C., O'Neill, N. T. and Slutsker, I.: Characterization of the optical properties of biomass burning aerosols in Zambia during the 1997 ZIBBEE field campaign, J. Geophys. Res. Atmos., 106(D4), 3425–3448, doi:10.1029/2000JD900555, 2001.
775
Eck, T. F., Holben, B. N., Ward, D. E., Mukelabai, M. M., Dubovik, O., Smirnov, A., Schafer, J. S., Hsu, N. C., Piketh, S. J., Queface, A., Le Roux, J., Swap, R. J. and Slutsker, I.: Variability of biomass burning aerosol optical characteristics in southern Africa during the SAFARI 2000 dry season campaign and a comparison of single scattering albedo estimates from radiometric measurements, J. Geophys. Res. Atmos., 108(D13), 1–21, 2003.
780
Eck, T. F., Holben, B. N., Reid, J. S., Mukelabai, M. M., Piketh, S. J., Torres, O., Jethva, H. T., Hyer, E. J., Ward, D. E., Dubovik, O., Sinyuk, A., Schafer, J. S., Giles, D. M., Sorokin, M., Smirnov, A. and Slutsker, I.: A seasonal trend of single scattering albedo in southern African biomass-burning particles: Implications for satellite products and estimates of emissions for the world's largest biomass-burning source, J. Geophys. Res. Atmos.,
785 118(12), 6414–6432, doi:10.1002/jgrd.50500, 2013.

Fraser, R. S. and Kaufman, Y. J.: The Relative Importance of Aerosol Scattering and Absorption in Remote Sensing, IEEE Trans. Geosci. Remote Sens., GE-23(5), 625–633, doi:10.1109/TGRS.1985.289380, 1985.

790 Hansen, J., Sato, M. and Ruedy, R.: Radiative forcing and climate response, J. Geophys. Res. Atmos., 102(D6), 6831–6864, doi:10.1029/96JD03436, 1997.

Heintzenberg, J., Charlson, R. J., Clarke, A. D., Liousse, C., Ramaswamy, V., Shine, K. P., Wendisch, M. and Helas, G.: Measurements and modelling of aerosol single-scattering albedo: Progress, problems and prospects., in
795 Contributions to Atmospheric Physics, vol. 70, pp. 249–263., 1997.

Herman, B. M. and Browning, S. R.: A Numerical Solution to the Equation of Radiative Transfer, J. Atmos. Sci., 22(5), 559–566, doi:10.1175/1520-0469(1965)022<0559:anstte>2.0.co;2, 1965.

800   Holben, B. N., Eck, T. F., Slutsker, I., Tanré, D., Buis, J. P., Setzer, A., Vermote, E., Reagan, J. A., Kaufman, Y. J., Nakajima, T., Lavenu, F., Jankowiak, I. and Smirnov, A.: AERONET - A federated instrument network and data archive for aerosol characterization, Remote Sens. Environ., 66(1), 1–16, doi:10.1016/S0034-4257(98)00031-5, 1998.

805   van de Hulst, H. C.: Light scattering by small particles, John Wiley and Sons, New York., 1957.

Ilias., F., Natis, A., Siomos, N., Drosoglou, T. and Bais, A. F.: Deriving Aerosol Absorption Properties from Solar Ultraviolet Radiation Spectral Measurements at Thessaloniki, Greece, Remote Sens., 11(18), 1–26, doi:10.3390/rs11182179, 2019.

810

IPCC: Intergovernmental Panel on Climate Change: The Physical Science Basis: Contribution of Working Group I to the Fifth Assessment Report of the Intergovernmental Panel on Climate Change, in Climate Change, edited by T. F. Stocker, D. Qin, G. K. Plattner, M. Tignor, S. K. Allen, J. Boschung, A. Nauels, Y. Xia, V. Bex, and P. M. Midgley, p. 1535, Cambridge University Press., 2013.

815

Jethva, H. and Torres, O.: Satellite-based evidence of wavelength-dependent aerosol absorption in biomass burning smoke inferred from Ozone Monitoring Instrument, Atmos. Chem. Phys., 11(20), 10541–10551, doi:10.5194/acp-11-10541-2011, 2011.

820   Jethva, H., Torres, O. and Ahn, C.: Global assessment of OMI aerosol single-scattering albedo using ground-based AERONET inversion, J. Geophys. Res. Atmos., 119, 9020–9040, doi:10.1002/2014JD021672, 2014.

Kaufman, Y. J.: Satellite sensing of aerosol absorption., J. Geophys. Res. Atmos., 92(D4), 4307–4317, doi:10.1029/JD092iD04p04307, 1987.

825

Kaufman, Y. J., Martins, J. V., Remer, L. A., Schoeberl, M. R. and Yamasoe, M. A.: Satellite retrieval of aerosol absorption over the oceans using sunglint, Geophys. Res. Lett., 29(19), 1–4, doi:10.1029/2002gl015403, 2002.

Kirchstetter, T. W., Novakov, T. and Hobbs, P. V.: Evidence that the spectral dependence of light absorption by 830   aerosols is affected by organic carbon, J. Geophys. Res. D Atmos., 109(D21208), 1–12, doi:10.1029/2004JD004999, 2004.

Lee, K. H., Li, Z., Wong, M. S., Xin, J., Wang, Y., Hao, W. M. and Zhao, F.: Aerosol single scattering albedo estimated across China from a combination of ground and satellite measurements, J. Geophys. Res. Atmos., 835   112(D22S15), 1–17, doi:10.1029/2007JD009077, 2007.

Levelt, P. F., Van Den Oord, G. H. J., Dobber, M. R., Mälkki, A., Visser, H., De Vries, J., Stammes, P., Lundell, J. O. V. and Saari, H.: The ozone monitoring instrument, IEEE Trans. Geosci. Remote Sens., 44(5), 1093–1101, doi:10.1109/TGRS.2006.872333, 2006.

840

Li, X., Christopher, S. A., Zhang, J., Chou, J. and Welch, R. M.: Aerosol single-scattering albedo estimated from NOAA-14 AVHRR measurements: case studies over Brazil, in Proc. SPIE 3756, Optical Spectroscopic Techniques and Instrumentation for Atmospheric and Space Research III., 1999.

845   Li, Z., Zhao, X., Kahn, R., Mishchenko, M., Remer, L., Lee, K. H., Wang, M., Laszlo, I., Nakajima, T. and

Maring, H.: Uncertainties in satellite remote sensing of aerosols and impact on monitoring its long-term trend: A review and perspective, Ann. Geophys., 27, 2755–2770, doi:10.5194/angeo-27-2755-2009, 2009.

850   Lyapustin, A. and Wang, Y.: MCD19A1 MODIS/Terra+Aqua Land Surface BRF Daily L2G Global 500m and 1km SIN Grid V006 [Dataset], NASA EOSDIS L. Process. DAAC, doi:10.5067/MODIS/MCD19A1.006, 2018.

Lyapustin, A., Smirnov, A., Holben, B., Chin, M., Streets, D. G., Lu, Z., Kahn, R., Slutsker, I., Laszlo, I., Kondragunta, S., Tanré, D., Dubovik, O., Goloub, P., Chen, H.-B., Sinyuk, A., Wang, Y. and Korkin, S.: Reduction of aerosol absorption in Beijing since 2007 from MODIS and AERONET, Geophys. Res. Lett., 855   38(10), 1–5, doi:10.1029/2011gl047306, 2011.

Malm, W. C.: Characteristics and origins of haze in the continental United States, Earth Sci. Rev., 33(1), 1–36, doi:10.1016/0012-8252(92)90064-Z, 1992.

860   Moosmüller, H., Chakrabarty, R. K. and Arnott, W. P.: Aerosol light absorption and its measurement: A review, J. Quant. Spectrosc. Radiat. Transf., 110(11), 844–878, doi:10.1016/j.jqsrt.2009.02.035, 2009.

Müller, T., Schladitz, A., Massling, A., Kaaden, N., Kandler, K. and Wiedensohler, A.: Spectral absorption coefficients and imaginary parts of refractive indices of Saharan dust during SAMUM-1, Tellus, Ser. B Chem. Phys. Meteorol., 61(1), 79–95, doi:10.1111/j.1600-0889.2008.00399.x, 2009.
865

Nakajima, T., Tonna, G., Rao, R., Boi, P., Kaufman, Y. and Holben, B.: Use of sky brightness measurements from ground for remote sensing of particulate polydispersions, Appl. Opt., 35(15), 2672–2686, doi:10.1364/ao.35.002672, 1996.
870
Onyeuwaoma, N. D., Nwofor, O. K., Chineke, T. C., Eguaroje, E. O. and Dike, V. N.: Implications of MODIS impression of aerosol loading over urban and rural settlements in Nigeria: Possible links to energy consumption patterns in the country, Atmos. Pollut. Res., 6(3), 484–494, doi:10.5094/APR.2015.054, 2015.

875   Petzold, A., Rasp, K., Weinzierl, B., Esselborn, M., Hamburger, T., Dörnbrack, A., Kandler, K., Schütz, L., Knippertz, P., Fiebig, M. and Virkkula, A.: Saharan dust absorption and refractive index from aircraft-based observations during SAMUM 2006, Tellus, Ser. B Chem. Phys. Meteorol., 61(1), 118–130, doi:10.1111/j.1600-0889.2008.00383.x, 2009.

880   Reid, J. S. and Hobbs, P. V.: Physical and optical properties of young smoke from individual biomass fires in Brazil, J. Geophys. Res. Atmos., 103(D24), 32013–32030, doi:10.1029/98JD00159, 1998.

Reid, J. S., Hobbs, P. V., Ferek, R. J., Blake, D. R., Martins, J. V., Dunlap, M. R. and Liousse, C.: Physical, chemical, and optical properties of regional hazes dominated by smoke in Brazil, J. Geophys. Res. Atmos., 885   103(D24), 32059–32080, doi:10.1029/98JD00458, 1998.

Satheesh, S. K. and Srinivasan, J.: A method to infer short wave absorption due to aerosols using satellite remote sensing, Geophys. Res. Lett., 32(13), 1–4, doi:10.1029/2005GL023064, 2005.

890   Schenkeveld, V. M. E., Jaross, G., Marchenko, S., Haffner, D., Kleipool, Q. L., Rozemeijer, N. C., Pepijn Veefkind, J. and Levelt, P. F.: In-flight performance of the Ozone Monitoring Instrument, Atmos. Meas. Tech.,

10(5), 1957–1986, doi:10.5194/amt-10-1957-2017, 2017.

Schnaiter, M., Schmid, O., Petzold, A., Fritzsche, L., Klein, K. F., Andreae, M. O., Helas, G., Thielmann, A.,
895   Gimmler, M., Möhler, O., Linke, C. and Schurath, U.: Measurement of wavelength-resolved light absorption by
aerosols utilizing a UV-VIS extinction cell, Aerosol Sci. Technol., 39(3), 249–260,
doi:10.1080/027868290925958, 2005.

Sinyuk, A., Torres, O. and Dubovik, O.: Combined use of satellite and surface observations to infer the imaginary
900   part of refractive index of Saharan dust, Geophys. Res. Lett., 30(2), 1–4, doi:10.1029/2002GL016189, 2003.

Sinyuk, A., Holben, B. N., Eck, T. F., M. Giles, D., Slutsker, I., Korkin, S., S. Schafer, J., Smirnov, A., Sorokin,
M. and Lyapustin, A.: The AERONET Version 3 aerosol retrieval algorithm, associated uncertainties and
comparisons to Version 2, Atmos. Meas. Tech., 13(6), 3375–3411, doi:10.5194/amt-13-3375-2020, 2020.
905
Sokolik, I. N. and Toon, O. B.: Incorporation of mineralogical composition into models of the radiative properties
of mineral aerosol from UV to IR wavelengths, J. Geophys. Res. Atmos., 104(D8), 9423–9444,
doi:10.1029/1998JD200048, 1999.

910   Torres, O., Bhartia, P. K., Herman, J. R., Ahmad, Z. and Gleason, J.: Derivation of aerosol properties from
satellite measurements of backscattered ultraviolet radiation: Theoretical basis, J. Geophys. Res. Atmos.,
103(D14), 17099–17110, doi:10.1029/98JD00900, 1998.

Torres, O., Herman, J. R., Bhartia, P. K. and Sinyuk, A.: Aerosol properties from EP-TOMS near UV
915   observations, Adv. Sp. Res., 29(11), 1771–1780, doi:10.1016/S0273-1177(02)00109-6, 2002.

Torres, O., Tanskanen, A., Veihelmann, B., Ahn, C., Braak, R., Bhartia, P. K., Veefkind, P. and Levelt, P.:
Aerosols and surface UV products form Ozone Monitoring Instrument observations: An overview, J. Geophys.
Res. Atmos., 112(D24), 1–14, doi:10.1029/2007JD008809, 2007.
920
Torres, O., Ahn, C. and Chen, Z.: Improvements to the OMI near-UV aerosol algorithm using A-train CALIOP
and AIRS observations, Atmos. Meas. Tech., 6(11), 3257–3270, doi:10.5194/amt-6-3257-2013, 2013.

Torres, O., Bhartia, P. K., Jethva, H. and Ahn, C.: Impact of the ozone monitoring instrument row anomaly on the
925   long-term record of aerosol products, Atmos. Meas. Tech., 11(5), 2701–2715, doi:10.5194/amt-11-2701-2018,
2018.

Vanderlei Martins, J., Artaxo, P., Kaufman, Y. J., Castanho, A. D. and Remer, L. A.: Spectral absorption
properties of aerosol particles from 350-2500nm, Geophys. Res. Lett., 36(13), 1–5, doi:10.1029/2009GL037435,
930   2009.

Ward, D. E.: Smoke and fire characteristics for cerrado and deforestation burns in Brazil: BASE-B experiment, J.
Geophys. Res., 97(D13), 14601–14619, doi:10.1029/92jd01218, 1992.

935   Zhu, L., Martins, J. V. and Remer, L. A.: Biomass burning aerosol absorption measurements with MODIS using
the critical reflectance method, J. Geophys. Res. Atmos., 116(D7), 1–15, doi:10.1029/2010JD015187, 2011.

Tables

Table 1: Description of the ground and satellite data products used in this work.

Purpose	Instrument	Product	Level & Version	Parameter(s)
For SSA retrieval in this work	AERONET	AOD	L2, V3	AOD and extinction angstrom exponent.
		Inversion	L2, V2	Particle size distributions, and real part of refractive index at 440 nm.
	OMI	OMLERWAVE, OMAERUV	L2, V1.8.9.1	TOA reflectances (with QFs), Aerosol type, LER, Aerosol layer height obtained from CALIPSO.
	MODIS	MYD04	L2, C006	TOA reflectances (with QFs) provided by Deep-Blue algorithm.
		MAIAC - MCD19A1	L2, C006	Surface reflectance at 466 and 646 nm.
Comparison	AERONET	Inversion	L2, V3	SSA at 440 and 675 nm.

945

Table 2: Estimated uncertainty in the retrieval of aerosol SSA due an error in surface reflectance of ± 0.01.

		$\tau_{440} = 0.2$		$\tau_{440} = 0.4$	
		340 nm	646 nm	340 nm	646 nm
Carbonaceous	± 0.01 Surf. Albedo	±0.010	±0.045	±0.005	±0.031
	± 1 km ALH	±0.025	±0.005	±0.014	±0.001
	± 0.02 AOD	±0.004	±0.040	±0.001	±0.018
Dust	± 0.01 Surf. Albedo	±0.027	±0.049	±0.011	±0.020
	± 1 km ALH	±0.034	±0.003	±0.019	±0.001
	± 0.02 AOD	±0.006	±0.036	±0.004	±0.018
Urban	± 0.01 Surf. Albedo	±0.017	±0.072	±0.011	±0.046
	+ 1 km ALH	0.009	0.0004	0.004	0.0003
	± 0.02 AOD	±0.006	±0.062	±0.004	±0.028

Table 3: Retrieved seasonal average SSA at 340, 354, 388, 466 and 646 nm and AAE at UV-Visible wavelength pairs for Carbonaceous, Dust, and Urban aerosols with observations $\tau_{440} > 0.4$ over individual AERONET sites from 2005 – 2016. Abbreviations used: AType is the aerosol type, NDays is the number of independent days, and NObs is the number of observations.

Site	AType	Season	NDays	NObs		τ_{440}	$\alpha_{440\text{-}870}$	Average SSA(λ)					Average AAE		
				OMI	MOD			340	354	388	466	646	354_388	466_646	340_646
Western USA															
Missoula	Carbon.	JJA	5	9	51	1.23	1.78	0.886	0.902	0.911	0.935	0.904	3.71	1.11	1.72
Missoula	Urban	JJA	10	26	83	0.70	1.91	0.871	0.874	0.869	0.870	0.847	1.56	1.47	1.68
Rimrock	Urban	SON	8	21	60	0.56	1.96	0.843	0.840	0.823	0.862	0.829	0.91	1.53	1.76
Rimrock	Urban	JJA	6	38	25	0.54	1.96	0.879	0.891	0.892	0.892	0.866	2.35	0.83	1.91
Sioux_Falls	Urban	JJA	8	41	98	0.46	1.51	0.928	0.944	0.950	0.940	0.879	4.28	-0.78	0.94
Eastern USA															
BONDVILLE	Urban	JJA	12	54	130	0.49	1.86	0.941	0.941	0.941	0.932	0.890	3.55	-0.03	1.18
GSFC	Urban	MAM	8	36	67	0.49	1.52	0.923	0.940	0.940	0.934	0.940	2.65	2.22	1.70
GSFC	Urban	JJA	10	51	27	0.47	1.78	0.950	0.954	0.962	0.948	0.927	4.81	0.55	1.70
MD_Science_Center	Urban	MAM	8	53	69	0.49	1.76	0.939	0.943	0.944	0.949	0.902	2.38	-0.33	0.79
MD_Science_Center	Urban	JJA	8	49	64	0.51	1.89	0.929	0.933	0.940	0.911	0.867	5.62	0.73	1.62
SERC	Urban	JJA	5	13	22	0.47	1.81	0.960	0.964	0.972	0.949	0.866	5.43	-1.86	0.64
Wallops	Urban	JJA	8	19	17	0.64	1.78	0.894	0.894	0.888	0.887	0.848	1.81	1.23	0.97
Mexico & Atlantic Islands															
Mexico_City	Urban	DJF	53	225	257	0.56	1.70	0.882	0.879	0.877	0.850	0.844	2.22	2.14	1.27
Mexico_City	Urban	MAM	31	67	78	0.67	1.68	0.904	0.909	0.914	0.857	0.832	5.13	1.47	0.95
Mexico_City	Urban	SON	6	13	13	0.47	1.67	0.875	0.864	0.849	0.842	0.804	0.57	1.01	0.94
South America															
Alta_Floresta	Carbon.	JJA	10	67	94	0.85	1.89	0.901	0.905	0.920	0.932	0.910	4.77	1.35	1.77
Alta_Floresta	Carbon.	SON	10	50	155	1.00	1.81	0.925	0.928	0.942	0.940	0.917	4.32	1.82	1.73
Alta_Floresta	Urban	SON	7	15	66	0.62	1.69	0.918	0.932	0.937	0.931	0.878	1.97	0.70	0.83
CUIABA-MIRANDA	Carbon.	JJA	6	40	61	0.70	1.75	0.882	0.887	0.909	0.898	0.870	4.73	1.17	2.06
CUIABA-MIRANDA	Carbon.	SON	23	164	283	0.94	1.76	0.899	0.906	0.918	0.913	0.880	3.57	0.88	1.37
CUIABA-MIRANDA	Urban	JJA	7	36	103	0.56	1.77	0.875	0.875	0.877	0.864	0.822	2.05	1.01	1.34

Atmospheric Measurement Techniques — Discussions — Open Access — EGU

Site	Type	Season												
	Urban	SON	27	217	448	0.54	1.75	0.905	0.914	0.922	0.875	3.96	0.93	1.36
Rio_Branco	Urban	JJA	8	47	127	0.53	1.83	0.897	0.901	0.924	0.887	2.51	0.84	1.64
Rio_Branco	Urban	SON	8	57	117	0.54	1.72	0.914	0.906	0.928	0.883	3.94	0.46	1.17
Ji_Parana_SE	Carbon.	JJA	7	23	42	0.86	1.83	0.919	0.921	0.932	0.914	3.07	1.84	1.70
Ji_Parana_SE	Urban	JJA	5	39	25	0.49	1.76	0.891	0.929	0.935	0.892	2.38	1.44	1.99
SANTA_CRUZ_UTEPSA	Urban	SON	15	79	230	0.56	1.67	0.887	0.900	0.929	0.905	1.99	0.94	1.75
SANTA_CRUZ_UTEPSA	Carbon.	SON	9	23	79	0.79	1.72	0.897	0.905	0.925	0.907	5.07	0.95	1.68
Sao_Paulo	Urban	SON	10	76	86	0.52	1.53	0.896	0.905	0.912	0.880	3.23	1.11	1.53
Europe														
Avignon	Mixt.	JJA	5	30	71	0.51	0.55	0.906	0.922	0.933	0.860	3.34	-2.26	-0.12
Avignon	Urban	JJA	7	41	53	0.51	1.60	0.924	0.934	0.939	0.861	2.63	0.36	0.61
Burjassot	Mixt.	JJA	14	73	71	0.50	0.67	0.896	0.900	0.911	0.881	2.66	-0.61	0.71
Barcelona	Mixt.	JJA	6	14	30	0.52	0.41	0.892	0.897	0.909	0.868	1.89	-1.56	0.37
Carpentras	Urban	MAM	5	12	70	0.46	1.41	0.909	0.927	0.919	0.850	0.09	0.90	0.82
Carpentras	Urban	JJA	8	42	106	0.46	1.69	0.926	0.937	0.942	0.822	3.99	0.49	0.70
FORTH_CRETE	Mixt.	MAM	6	38	130	0.46	0.56	0.890	0.904	0.916	0.851	1.94	-1.94	0.04
FORTH_CRETE	Mixt.	MAM	10	50	37	0.64	0.36	0.891	0.906	0.916	0.885	2.58	-0.08	0.25
FORTH_CRETE	Mixt.	MAM	7	31	42	0.58	0.35	0.894	0.909	0.928	0.952	3.71	-0.72	1.50
IMS-METU-ERDEMLI	Mixt.	JJA	11	45	28	0.51	0.88	0.887	0.896	0.899	0.888	2.09	1.40	0.89
Ispra	Urban	JJA	18	40	32	0.51	1.45	0.917	0.927	0.933	0.874	4.09	2.32	0.91
Ispra	Urban	SON	8	18	45	0.59	1.60	0.945	0.953	0.954	0.904	3.09	0.47	0.52
Ispra	Urban	SON	6	8	45	0.54	1.50	0.879	0.896	0.878	0.869	0.08	-0.69	1.18
Lecce_University	Mixt.	JJA	25	142	107	0.51	0.52	0.899	0.908	0.926	0.915	3.40	-1.19	0.96
Lecce_University	Urban	JJA	16	75	82	0.48	1.75	0.926	0.931	0.932	0.901	2.36	0.70	1.30
Lille	Urban	MAM	5	42	130	0.47	1.63	0.910	0.927	0.933	0.935	3.28	2.92	2.08
Lille	Urban	JJA	6	32	103	0.47	1.62	0.917	0.931	0.935	0.896	2.97	0.29	1.35
Minsk	Urban	MAM	5	20	118	0.47	1.64	0.923	0.945	0.951	0.906	3.53	1.40	1.50
Modena	Mixt.	MAM	7	29	112	0.55	0.92	0.900	0.911	0.919	0.870	2.29	-0.51	0.74
Modena	Mixt.	JJA	14	90	349	0.52	0.96	0.898	0.900	0.903	0.887	1.79	-0.94	0.85
Modena	Urban	MAM	24	156	621	0.48	1.54	0.911	0.916	0.914	0.892	1.46	0.92	1.09

Site	Type	Season												
Moldova	Urban	JJA	37	203	758	0.53	1.61	0.929	0.934	0.935	0.917	0.870	2.45	0.55	0.72
	Urban	SON	10	32	256	0.48	1.53	0.893	0.915	0.912	0.927	0.909	1.72	1.07	1.34
	Mixt.	MAM	6	46	191	0.50	0.66	0.878	0.899	0.913	0.950	0.907	2.52	-1.40	1.03
	Urban	JJA	14	64	230	0.48	1.74	0.922	0.926	0.919	0.929	0.909	1.04	1.33	1.55
Moscow_MSU_MO	Urban	MAM	8	95	182	0.48	1.53	0.895	0.907	0.908	0.911	0.891	3.38	1.29	1.37
	Mixt.	MAM	5	52	52	0.44	0.85	0.900	0.919	0.927	0.948	0.895	3.55	-1.16	1.14
	Urban	JJA	11	74	200	0.47	1.57	0.891	0.900	0.891	0.908	0.873	0.88	0.95	1.48
Palaiseau	Urban	MAM	6	31	70	0.47	1.56	0.925	0.938	0.940	0.938	0.920	2.30	1.20	1.48
	Urban	JJA	10	56	103	0.47	1.65	0.913	0.917	0.919	0.937	0.891	2.77	0.15	1.65
Rome_Tor_Vergata	Mixt.	MAM	6	32	41	0.48	0.46	0.906	0.923	0.935	0.933	0.873	2.80	-1.69	-0.07
	Mixt.	JJA	11	93	198	0.46	0.53	0.894	0.901	0.914	0.933	0.891	2.97	-0.66	0.59
	Urban	MAM	7	33	47	0.47	1.45	0.910	0.924	0.924	0.926	0.896	1.58	1.17	1.06
	Urban	JJA	19	70	166	0.47	1.62	0.920	0.923	0.920	0.920	0.863	1.40	2.10	0.85
Thessaloniki	Mixt.	SON	6	49	123	0.48	1.11	0.900	0.910	0.908	0.868	0.863	1.51	1.18	0.61
	Mixt.	JJA	13	119	198	0.53	0.66	0.911	0.918	0.926	0.946	0.896	1.87	-1.34	0.83
	Mixt.	MAM	5	26	33	0.53	1.01	0.909	0.927	0.932	0.926	0.916	2.55	1.11	1.07
	Urban	SON	7	36	104	0.50	1.42	0.863	0.856	0.837	0.810	0.799	0.13	1.42	0.70
	Urban	JJA	35	130	200	0.51	1.64	0.932	0.936	0.936	0.910	0.905	2.89	2.12	0.99
Toulon	Mixt.	JJA	5	31	41	0.49	0.81	0.896	0.918	0.925	0.928	0.893	3.00	-0.21	0.88
Sahel															
Banizoumbou	Dust	DJF	17	151	184	0.76	0.13	0.930	0.933	0.943	0.956	0.970	2.16	1.90	1.60
	Dust	MAM	155	1525	1458	0.78	0.13	0.895	0.907	0.930	0.934	0.956	4.18	2.07	2.02
	Dust	JJA	54	405	519	0.65	0.10	0.882	0.899	0.925	0.925	0.952	3.87	2.01	1.88
	Dust	SON	19	164	89	0.52	0.17	0.915	0.927	0.943	0.937	0.956	3.80	1.87	1.59
	Mixt.	SON	51	370	1179	0.50	0.37	0.925	0.936	0.951	0.941	0.908	4.75	-1.02	0.11
	Mixt.	JJA	16	97	287	0.50	0.37	0.879	0.897	0.914	0.927	0.908	4.06	-0.12	1.20
	Mixt.	MAM	67	674	950	0.66	0.25	0.907	0.918	0.939	0.945	0.931	4.64	-0.06	1.18
	Mixt.	DJF	116	946	3120	0.67	0.47	0.908	0.912	0.923	0.936	0.933	2.50	0.52	1.50
Dakar	Dust	DJF	21	117	132	0.65	0.14	0.911	0.914	0.925	0.948	0.977	2.25	3.28	2.55
	Dust	MAM	85	531	573	0.76	0.13	0.882	0.893	0.917	0.929	0.974	3.69	4.12	3.08
	Dust	JJA	51	239	323	0.80	0.10	0.865	0.881	0.910	0.932	0.971	3.84	3.48	2.72

Open Access — EGU

Site	Type	Season													
IER_Cinzana	Dust	SON	6	19	9	0.79	0.10	0.901	0.913	0.929	0.936	0.958	2.53	1.78	1.74
	Mixt.	DJF	63	367	423	0.60	0.51	0.891	0.898	0.912	0.922	0.957	2.65	3.17	2.38
	Mixt.	MAM	57	341	306	0.55	0.34	0.892	0.903	0.903	0.936	0.970	4.17	3.67	2.67
	Mixt.	SON	13	48	90	0.55	0.46	0.909	0.913	0.927	0.914	0.895	3.38	-0.04	0.76
	Mixt.	JJA	7	22	38	0.49	0.37	0.920	0.934	0.935	0.943	0.949	3.86	1.51	2.32
	Mixt.	MAM	44	327	389	0.58	0.30	0.887	0.895	0.912	0.923	0.953	3.17	2.75	2.19
	Mixt.	DJF	93	732	1383	0.65	0.49	0.892	0.895	0.903	0.919	0.949	1.69	2.68	2.28
	Dust	SON	20	154	232	0.60	0.13	0.897	0.907	0.918	0.934	0.959	1.67	2.03	1.38
	Dust	JJA	49	294	284	0.71	0.09	0.867	0.882	0.913	0.938	0.973	3.84	3.72	3.05
	Dust	MAM	93	900	976	0.83	0.12	0.882	0.889	0.908	0.929	0.969	2.54	3.59	2.78
	Dust	DJF	26	228	328	0.73	0.13	0.904	0.907	0.919	0.936	0.969	1.71	3.18	2.50
Ilorin	Mixt.	SON	26	209	481	0.51	0.34	0.921	0.930	0.940	0.935	0.943	3.50	-0.34	0.63
	Dust	MAM	7	93	138	1.18	0.15	0.873	0.885	0.906	0.922	0.941	2.67	1.17	1.34
	Mixt.	DJF	295	2798	8709	1.17	0.68	0.887	0.889	0.894	0.901	0.934	1.39	0.84	1.12
	Mixt.	MAM	63	545	822	0.83	0.34	0.894	0.906	0.925	0.922	0.902	4.24	1.53	1.38
	Mixt.	SON	38	346	864	0.62	0.66	0.897	0.901	0.908	0.921	0.934	1.98	-0.79	0.47
	Carbon.	DJF	19	77	259	1.06	1.33	0.865	0.864	0.871	0.866	0.883	1.62	1.29	1.38
	Urban	DJF	37	259	1215	0.85	1.30	0.864	0.862	0.858	0.855	0.859	1.02	1.51	1.30
	Urban	SON	5	62	188	0.55	1.31	0.863	0.868	0.869	0.852	0.841	1.55	1.38	1.19
Ouagadougou	Dust	DJF	6	110	231	1.31	0.09	0.892	0.898	0.912	0.930	0.962	1.62	2.22	1.52
	Dust	MAM	19	240	345	0.87	0.13	0.893	0.901	0.919	0.924	0.969	2.55	3.53	2.00
	Dust	JJA	11	72	128	0.93	0.09	0.889	0.903	0.930	0.929	0.961	3.95	2.44	2.07
	Mixt.	DJF	19	179	439	0.91	0.36	0.904	0.906	0.915	0.936	0.962	1.55	2.74	2.44
	Mixt.	SON	6	81	144	0.66	0.33	0.925	0.931	0.938	0.932	0.939	2.52	1.25	0.77
Zinder_Airport	Dust	MAM	34	399	362	0.80	0.13	0.882	0.894	0.914	0.940	0.981	2.83	4.63	3.56
	Dust	JJA	26	209	129	0.65	0.09	0.872	0.890	0.921	0.947	0.987	4.47	5.68	3.97
	Dust	DJF	22	207	265	0.58	0.55	0.888	0.894	0.908	0.942	0.983	2.35	5.20	3.49
	Mixt.	MAM	22	195	161	0.61	0.27	0.876	0.887	0.905	0.951	0.980	2.24	4.59	3.57
	Mixt.	JJA	6	47	28	0.53	0.27	0.895	0.915	0.934	0.958	0.967	3.31	2.10	1.91
	Mixt.	SON	15	88	183	0.52	0.38	0.904	0.916	0.929	0.938	0.965	3.31	2.69	1.85
Agoufou	Dust	DJF	14	108	207	0.81	0.11	0.922	0.924	0.936	0.951	0.968	2.30	2.06	1.78

Atmospheric Measurement Techniques Discussions — Open Access — EGU

Region / Site	Type	Season	(1)	(2)	(3)	(4)	(5)	(6)	(7)	(8)	(9)	(10)	(11)	(12)
Southern Africa	Dust	MAM	86	908	991	0.79	0.12	0.897	0.908	0.934	0.957	3.30	2.07	1.87
	Dust	JJA	70	568	914	0.69	0.09	0.893	0.904	0.926	0.950	3.64	1.94	1.59
	Dust	SON	18	140	207	0.63	0.12	0.898	0.911	0.931	0.955	3.56	1.52	1.71
	Mixt.	DJF	33	335	932	0.63	0.43	0.915	0.921	0.934	0.924	3.01	0.26	0.81
	Mixt.	MAM	24	286	356	0.54	0.25	0.922	0.930	0.949	0.950	5.85	-0.02	0.64
	Mixt.	JJA	14	89	267	0.46	0.24	0.895	0.907	0.925	0.937	3.62	-0.73	0.31
	Mixt.	SON	26	197	524	0.50	0.37	0.928	0.938	0.953	0.947	5.09	-1.14	0.16
Mongu	Carbon.	JJA	25	156	328	0.77	1.83	0.852	0.851	0.859	0.881	2.44	0.96	1.73
	Carbon.	SON	21	182	448	1.08	1.79	0.863	0.867	0.879	0.905	2.96	0.87	1.61
	Urban	JJA	29	316	358	0.51	1.85	0.867	0.866	0.866	0.903	1.83	0.97	2.10
	Urban	SON	19	208	135	0.70	1.71	0.878	0.884	0.887	0.873	2.08	0.17	1.79
	Carbon.	SON	7	51	56	0.57	1.67	0.896	0.904	0.931	0.900	6.17	1.25	1.50
Skukuza	Urban	JJA	8	66	120	0.53	1.59	0.892	0.897	0.901	0.903	2.67	0.94	1.65
	Urban	SON	11	104	180	0.51	1.60	0.900	0.911	0.929	0.878	4.29	1.28	1.46
Mongu_Inn	Urban	JJA	14	44	70	0.64	1.74	0.842	0.845	0.852	0.864	2.38	3.56	2.73
	Urban	SON	27	141	354	0.90	1.78	0.855	0.853	0.848	0.849	1.50	4.06	2.93
Pretoria_CSIR-DPSS	Urban	JJA	5	40	64	0.50	1.50	0.858	0.863	0.873	0.886	2.43	1.57	2.11
	Urban	SON	7	70	113	0.43	1.48	0.861	0.864	0.870	0.873	2.35	1.60	1.82
Sahara	Dust	JJA	44	248	282	0.65	0.13	0.879	0.894	0.924	0.945	4.50	4.22	2.97
	Dust	SON	5	27	58	0.55	0.13	0.890	0.899	0.926	0.939	4.40	3.66	2.71
Saada	Dust	JJA	41	245	318	0.80	0.10	0.871	0.888	0.915	0.929	3.64	4.07	3.10
	Dust	MAM	22	160	241	0.77	0.16	0.865	0.887	0.914	0.928	3.70	4.02	3.27
	Mixt.	JJA	43	247	220	0.52	0.28	0.883	0.896	0.922	0.946	4.57	2.64	2.57
	Mixt.	MAM	8	55	129	0.61	0.29	0.875	0.892	0.908	0.942	2.39	0.69	1.66
Tamanrasset_INM	Dust	SON	7	19	30	0.74	0.10	0.875	0.891	0.915	0.938	3.50	4.45	2.86
	Dust	MAM	16	128	175	0.58	0.26	0.873	0.891	0.917	0.924	3.51	3.87	2.39
Arabian Peninsula	Mixt.	JJA	6	35	33	0.46	0.29	0.848	0.864	0.889	0.914	2.65	3.87	2.67
Nes_Ziona	Mixt.	MAM	14	91	73	0.48	0.45	0.889	0.903	0.918	0.919	3.18	0.02	1.01

Site	Type	Season														
SEDE_BOKER	Mixt.	JJA	11	84	57	0.51	0.87	0.914	0.922	0.933	0.924	0.926	3.01	1.41	1.57
	Mixt.	SON	7	38	31	0.55	0.98	0.897	0.909	0.919	0.936	0.928	2.48	0.54	1.66
	Urban	JJA	5	28	19	0.53	1.40	0.921	0.921	0.925	0.923	0.911	1.97	2.57	2.04
	Dust	MAM	13	98	52	0.77	0.10	0.895	0.909	0.938	0.960	0.984	5.53	3.54	3.31
	Mixt.	MAM	10	56	24	0.51	0.27	0.897	0.910	0.935	0.965	0.964	5.37	0.59	2.48
	Mixt.	JJA	8	36	13	0.57	0.48	0.896	0.911	0.936	0.963	0.978	4.48	2.90	3.12
	Dust	DJF	10	56	72	0.60	0.12	0.937	0.944	0.962	0.955	0.984	6.22	4.63	2.75
Solar_Village	Dust	MAM	5	47	9	0.93	0.06	0.898	0.909	0.934	0.969	0.991	3.64	4.35	4.29
	Dust	JJA	21	187	226	0.95	0.11	0.898	0.910	0.933	0.957	0.984	3.59	3.96	3.73
	Dust	SON	7	31	35	0.83	0.12	0.907	0.918	0.942	0.958	0.986	4.76	5.25	3.83
	Mixt.	JJA	28	202	81	0.61	0.40	0.901	0.912	0.933	0.959	0.981	4.08	4.47	3.79
	Mixt.	SON	9	64	48	0.49	0.50	0.914	0.925	0.939	0.958	0.979	3.59	3.98	2.58
	Mixt.	MAM	6	20	17	0.86	0.12	0.895	0.907	0.927	0.966	0.987	2.92	3.46	4.33
	Mixt.	DJF	9	52	124	0.66	0.78	0.885	0.893	0.897	0.904	0.903	1.43	1.63	1.49
Cairo_EMA_2	Mixt.	MAM	84	604	583	0.56	0.61	0.888	0.901	0.915	0.925	0.909	3.04	0.62	1.45
	Mixt.	JJA	103	557	800	0.51	0.89	0.887	0.896	0.905	0.929	0.904	2.40	0.59	1.41
	Mixt.	SON	29	151	215	0.53	0.88	0.877	0.885	0.890	0.914	0.897	1.88	0.71	1.66
	Carbon.	DJF	5	8	14	0.63	1.41	0.886	0.887	0.893	0.893	0.916	2.45	2.65	1.91
	Urban	DJF	11	50	114	0.63	1.34	0.877	0.877	0.869	0.855	0.874	0.97	2.68	1.83
	Urban	MAM	15	78	98	0.54	1.31	0.892	0.904	0.912	0.911	0.897	3.11	1.63	1.82
	Urban	JJA	52	166	291	0.52	1.30	0.885	0.893	0.895	0.901	0.869	1.82	0.82	1.45
	Urban	SON	24	72	150	0.60	1.33	0.874	0.879	0.877	0.899	0.893	1.44	2.03	2.01
Eastern Asia															
	Dust	MAM	11	81	184	1.10	0.10	0.876	0.899	0.914	0.918	0.941	2.76	1.56	1.37
Beijing	Mixt.	DJF	24	135	631	0.83	0.98	0.857	0.874	0.876	0.883	0.873	1.60	0.72	1.22
	Mixt.	MAM	95	731	1989	0.88	0.74	0.887	0.901	0.910	0.921	0.903	2.26	0.43	1.06
	Mixt.	JJA	12	60	198	0.61	0.71	0.882	0.900	0.903	0.908	0.862	1.49	-0.67	0.50
	Mixt.	SON	17	81	511	0.60	0.94	0.859	0.868	0.859	0.891	0.876	0.32	0.68	1.05
	Carbon.	DJF	40	178	509	0.98	1.34	0.868	0.879	0.886	0.897	0.890	2.29	1.30	1.78
	Carbon.	MAM	10	31	73	1.07	1.36	0.888	0.898	0.903	0.911	0.912	1.92	1.70	1.62
	Carbon.	SON	6	7	73	0.67	1.44	0.871	0.876	0.878	0.906	0.894	1.90	1.58	1.87

Atmospheric Measurement Techniques — Open Access — EGU — Discussions

Site	Type	Season												
Osaka	Urban	DJF	33	176	784	0.61	1.36	0.851	0.869	0.863	0.873	0.867	1.02	1.48	1.62
	Urban	MAM	41	233	835	0.65	1.42	0.885	0.898	0.899	0.899	0.899	1.81	1.55	1.71
	Urban	JJA	16	77	152	0.60	1.45	0.916	0.935	0.936	0.904	0.877	3.12	1.15	0.95
	Urban	SON	26	117	824	0.60	1.37	0.883	0.890	0.881	0.886	0.874	0.69	1.31	1.41
	Mixt.	MAM	32	193	294	0.62	0.82	0.897	0.907	0.907	0.924	0.895	3.37	0.04	0.92
Shirahama	Urban	MAM	24	118	210	0.56	1.48	0.901	0.908	0.910	0.900	0.864	2.03	0.83	1.09
	Urban	MAM	12	50	82	0.53	1.43	0.903	0.914	0.913	0.914	0.884	1.46	0.94	1.43
	Mixt.	MAM	17	55	88	0.58	0.81	0.907	0.923	0.936	0.924	0.867	4.49	-1.31	1.08
	Dust	MAM	9	81	141	1.12	0.08	0.874	0.896	0.912	0.938	0.958	1.95	1.86	1.78
XiangHe	Mixt.	DJF	22	142	631	0.82	0.91	0.872	0.889	0.898	0.909	0.905	2.14	0.76	1.36
	Mixt.	MAM	103	856	2582	0.84	0.81	0.893	0.905	0.914	0.930	0.923	2.27	0.95	1.45
	Mixt.	JJA	13	71	165	0.86	0.83	0.898	0.911	0.910	0.900	0.872	1.36	0.08	0.79
	Mixt.	SON	20	131	754	0.71	0.96	0.883	0.889	0.889	0.910	0.900	1.59	0.81	1.05
	Carbon.	DJF	39	209	783	0.81	1.35	0.869	0.886	0.896	0.908	0.905	2.65	1.35	1.90
	Carbon.	MAM	12	37	98	0.79	1.41	0.893	0.901	0.911	0.934	0.930	2.88	1.67	2.05
	Carbon.	JJA	5	19	35	0.96	1.36	0.919	0.931	0.946	0.948	0.938	4.29	1.46	1.85
	Carbon.	SON	12	31	129	0.65	1.30	0.880	0.888	0.894	0.928	0.923	1.98	1.21	2.28
	Urban	DJF	13	82	342	0.67	1.36	0.893	0.909	0.910	0.918	0.920	1.53	1.76	1.76
	Urban	MAM	31	215	717	0.64	1.41	0.902	0.911	0.914	0.931	0.921	1.96	1.51	1.83
	Urban	JJA	26	114	337	0.75	1.44	0.905	0.915	0.920	0.923	0.908	3.08	1.27	1.32
	Urban	SON	24	151	776	0.57	1.34	0.895	0.902	0.897	0.911	0.904	1.14	1.42	1.61
Northern India															
Kanpur	Dust	MAM	21	159	195	0.86	0.12	0.871	0.883	0.901	0.950	0.970	2.17	2.72	3.20
	Dust	JJA	8	67	29	0.84	0.08	0.887	0.901	0.913	0.954	0.970	2.14	2.13	2.48
	Mixt.	DJF	22	176	794	0.58	0.99	0.881	0.890	0.897	0.906	0.856	2.19	-0.13	0.76
	Mixt.	MAM	262	2027	5138	0.68	0.61	0.872	0.882	0.891	0.927	0.912	1.72	0.76	1.88
	Mixt.	JJA	39	290	335	0.68	0.48	0.891	0.905	0.915	0.956	0.928	2.23	-0.29	2.01
	Mixt.	SON	22	155	551	0.59	0.88	0.882	0.894	0.896	0.931	0.893	1.50	-0.34	1.02
	Carbon.	DJF	25	105	439	0.82	1.38	0.913	0.912	0.922	0.929	0.913	3.19	0.69	1.21
	Carbon.	SON	24	120	586	0.94	1.35	0.902	0.907	0.918	0.930	0.913	2.69	0.93	1.52
	Urban	DJF	29	151	1058	0.54	1.41	0.890	0.891	0.890	0.910	0.870	1.40	0.43	1.14

Site	Type	Season												
Jaipur	Urban	MAM	16	132	297	0.71	1.31	0.885	0.890	0.887	0.905	0.865	0.98	0.55	0.93
	Urban	SON	29	226	1097	0.59	1.38	0.896	0.901	0.904	0.908	0.863	1.78	0.44	1.10
	Dust	MAM	23	162	106	0.58	0.15	0.879	0.892	0.910	0.943	0.975	2.79	3.72	3.53
	Dust	JJA	7	60	15	0.53	0.14	0.890	0.906	0.920	0.957	0.974	2.26	2.87	3.35
	Mixt.	DJF	20	131	382	0.56	0.93	0.866	0.874	0.876	0.916	0.890	1.18	0.32	1.47
	Mixt.	JJA	23	148	76	0.54	0.46	0.883	0.901	0.910	0.940	0.929	1.87	0.56	1.77
	Mixt.	MAM	79	597	551	0.53	0.55	0.878	0.889	0.896	0.932	0.916	1.65	0.47	1.88
	Mixt.	SON	19	123	440	0.53	0.81	0.871	0.882	0.880	0.920	0.878	0.69	-0.09	1.12
	Urban	DJF	22	126	456	0.53	1.34	0.875	0.878	0.869	0.904	0.889	0.65	1.08	1.56
	Urban	SON	7	36	158	0.59	1.29	0.866	0.867	0.859	0.915	0.923	0.73	1.99	2.06
Gandhi_College	Mixt.	DJF	6	52	166	0.51	0.97	0.862	0.867	0.872	0.924	0.868	1.53	-0.57	1.18
	Mixt.	MAM	200	1391	4128	0.79	0.76	0.872	0.880	0.884	0.908	0.892	1.41	0.83	1.62
	Mixt.	JJA	32	163	355	0.79	0.60	0.884	0.893	0.899	0.939	0.923	1.54	0.19	1.71
	Mixt.	SON	7	31	127	0.54	0.65	0.899	0.919	0.937	0.946	0.886	4.25	-2.16	0.65
	Carbon.	SON	9	25	163	0.89	1.39	0.916	0.918	0.926	0.936	0.925	2.69	1.17	1.66
	Urban	DJF	7	56	264	0.54	1.42	0.892	0.896	0.893	0.902	0.869	1.18	0.80	1.15
	Urban	MAM	26	140	495	0.75	1.37	0.888	0.887	0.881	0.893	0.882	0.75	1.63	1.58
Australia	Urban	SON	9	59	231	0.55	1.38	0.890	0.901	0.906	0.901	0.836	2.05	0.06	0.87
Jabiru	Urban	SON	14	57	102	0.50	1.71	0.889	0.889	0.890	0.889	0.879	2.28	1.76	1.46
	Carbon.	SON	10	43	56	0.55	1.70	0.890	0.896	0.911	0.892	0.872	4.51	1.60	1.62
Lake_Argyle	Carbon.	SON	33	174	496	0.65	1.59	0.871	0.870	0.873	0.881	0.870	2.04	1.77	1.37
	Urban	SON	21	95	230	0.47	1.65	0.856	0.860	0.861	0.878	0.862	1.78	2.04	1.64
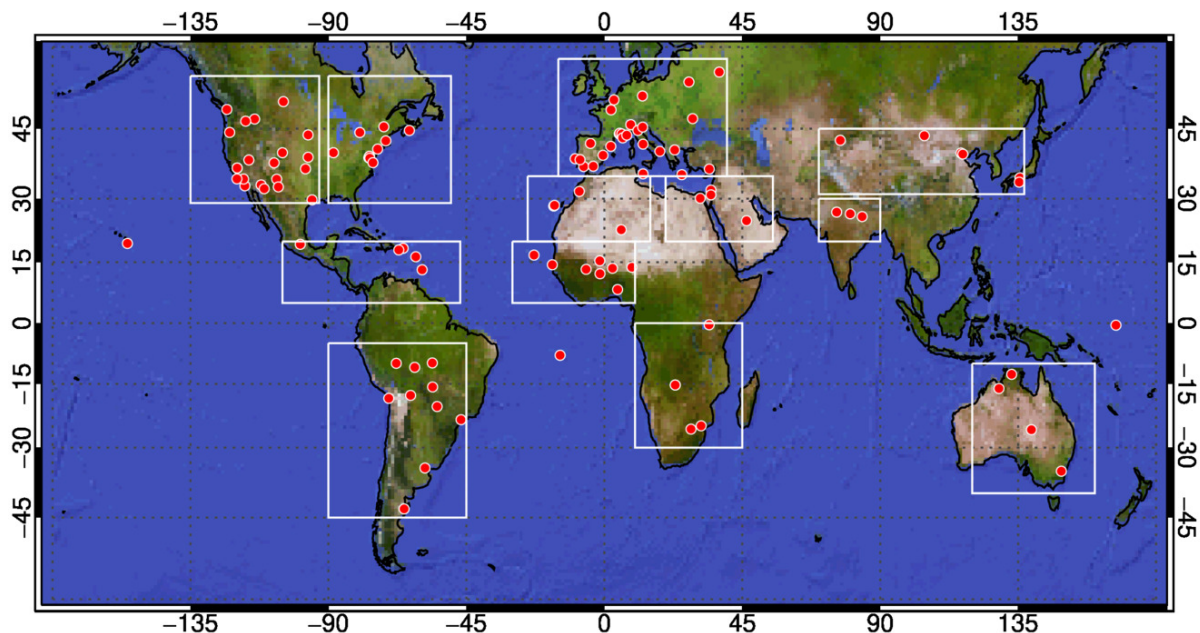
Figures

Figure 1: The geo-distribution of AERONET sites whose AOD data are used for the retrieval of spectral aerosol single scattering albedo in this work. The areas marked with white boxes are considered to develop regional representation of aerosol SSA.

965
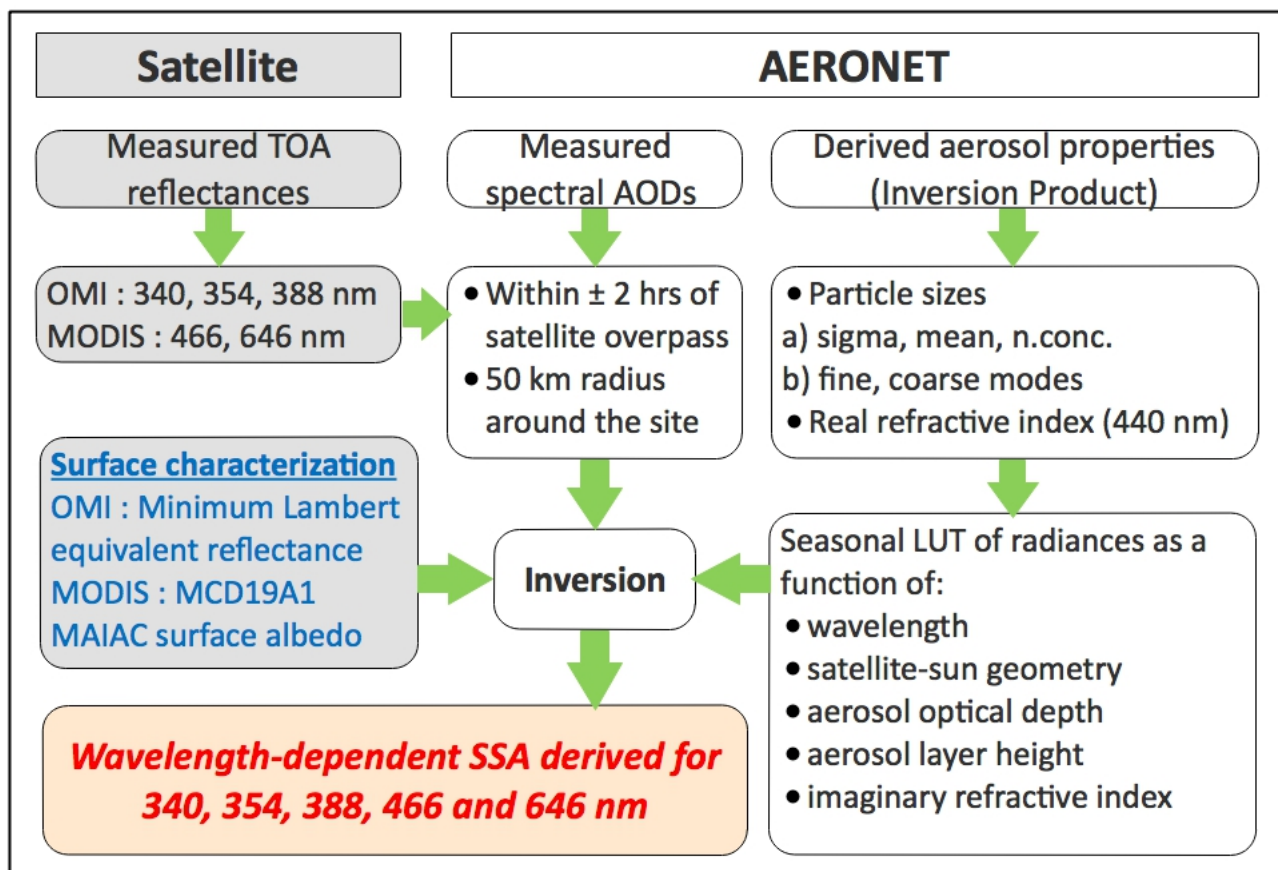
966
967 **Figure 2: Schematic flow chart of the methodology used to retrieve aerosol spectral single scattering**
968 **albedo.**
969
970

971
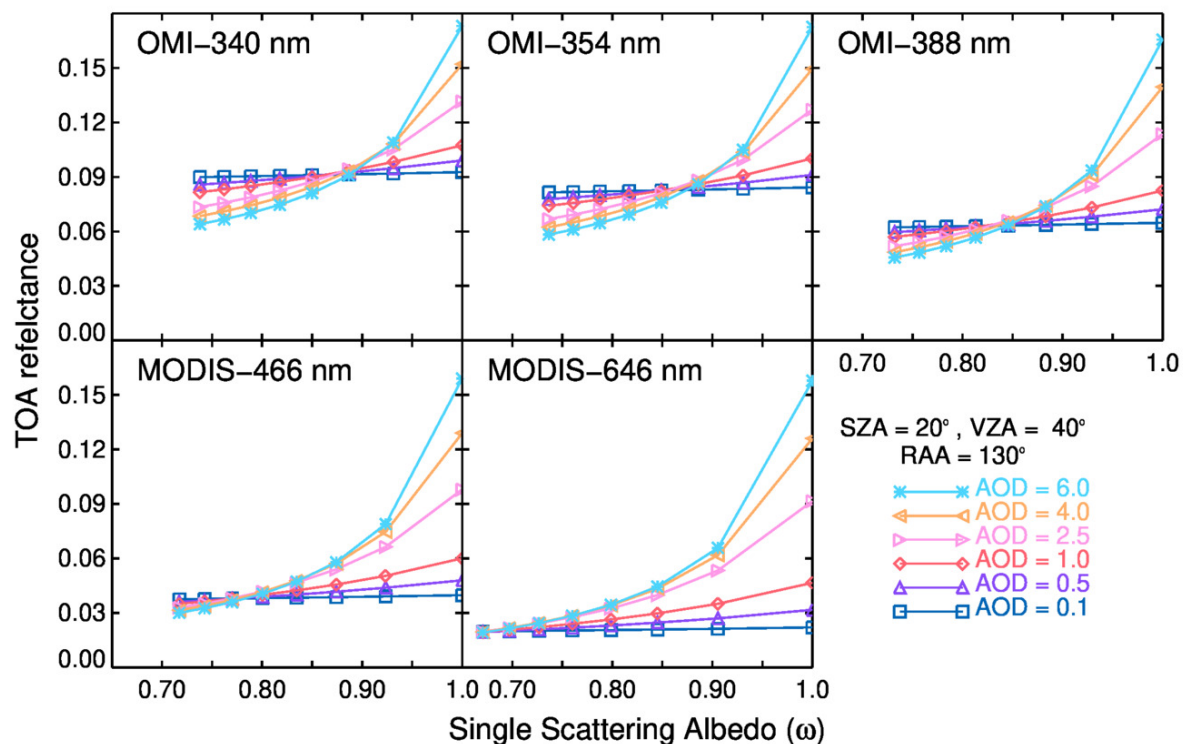
972
973 Figure 3: Simulated TOA radiances for the aerosols over the GSFC site as a function of τ and SSA in the
974 UV-Visible range.
975

975
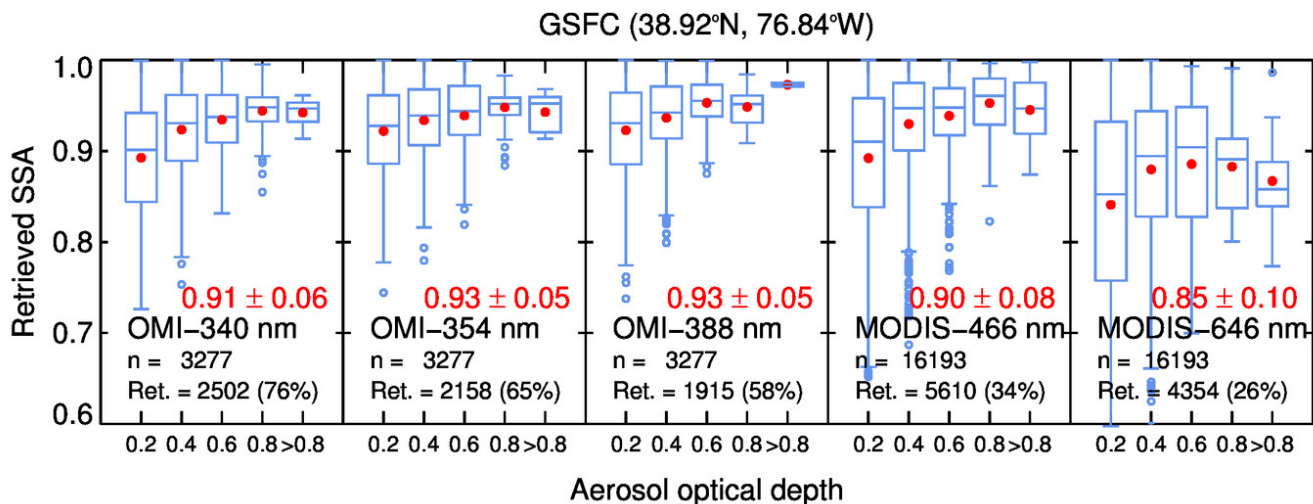
Figure 4: Retrieved aerosol SSA over the GSFC site for the satellite observations period of 2005 – 2016. Average and standard deviation of retrieved SSA for the entire range of AOD is shown in red. Abbreviations used: n is the number of satellite-AERONET collocated observations, and ret. is the number of observations for which SSA is retrieved.

980
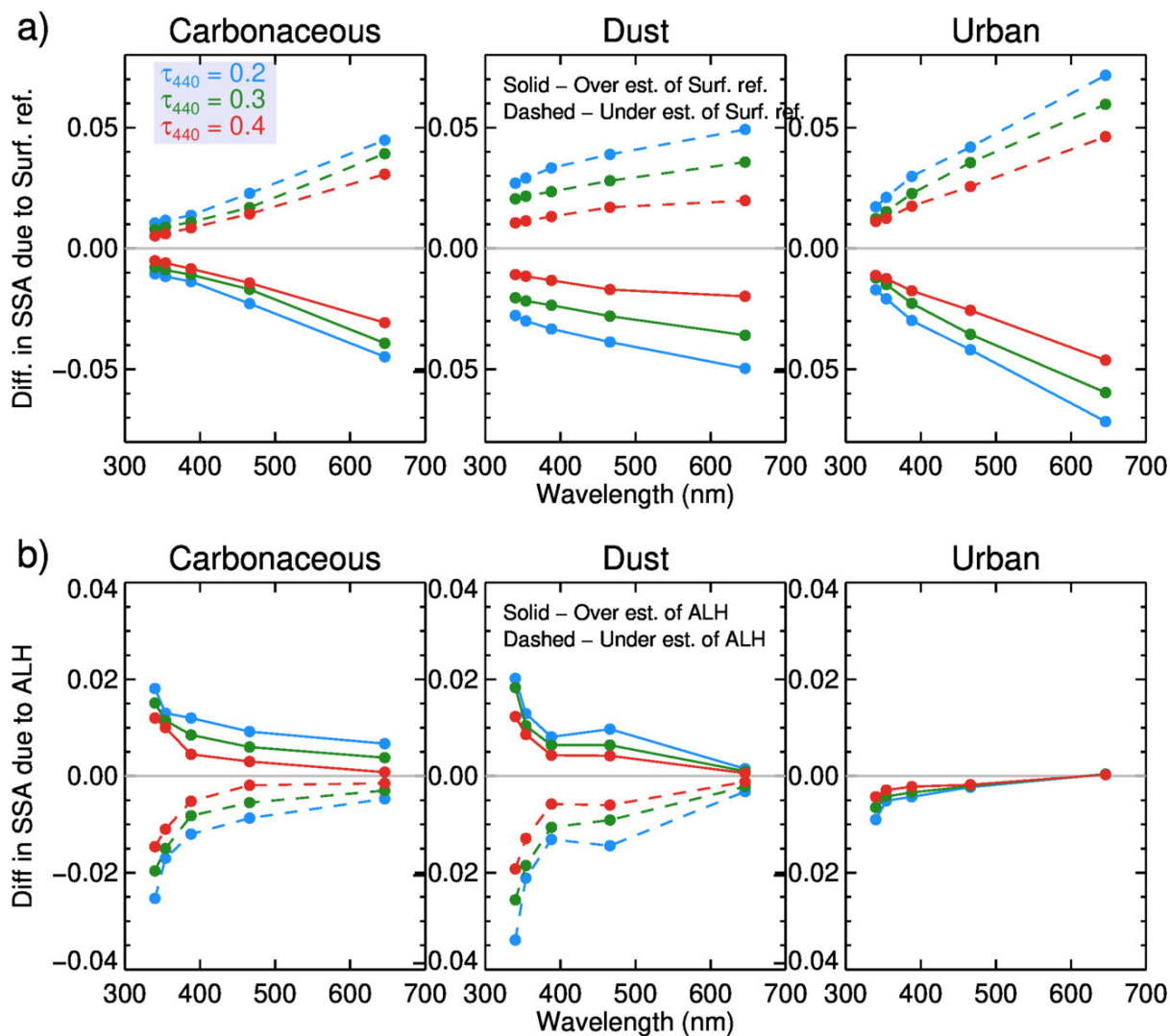
Figure 5: Uncertainty in SSA retrievals due to changes in (a) ±0.01 surface reflectance, and (b) ±1 km ALH.
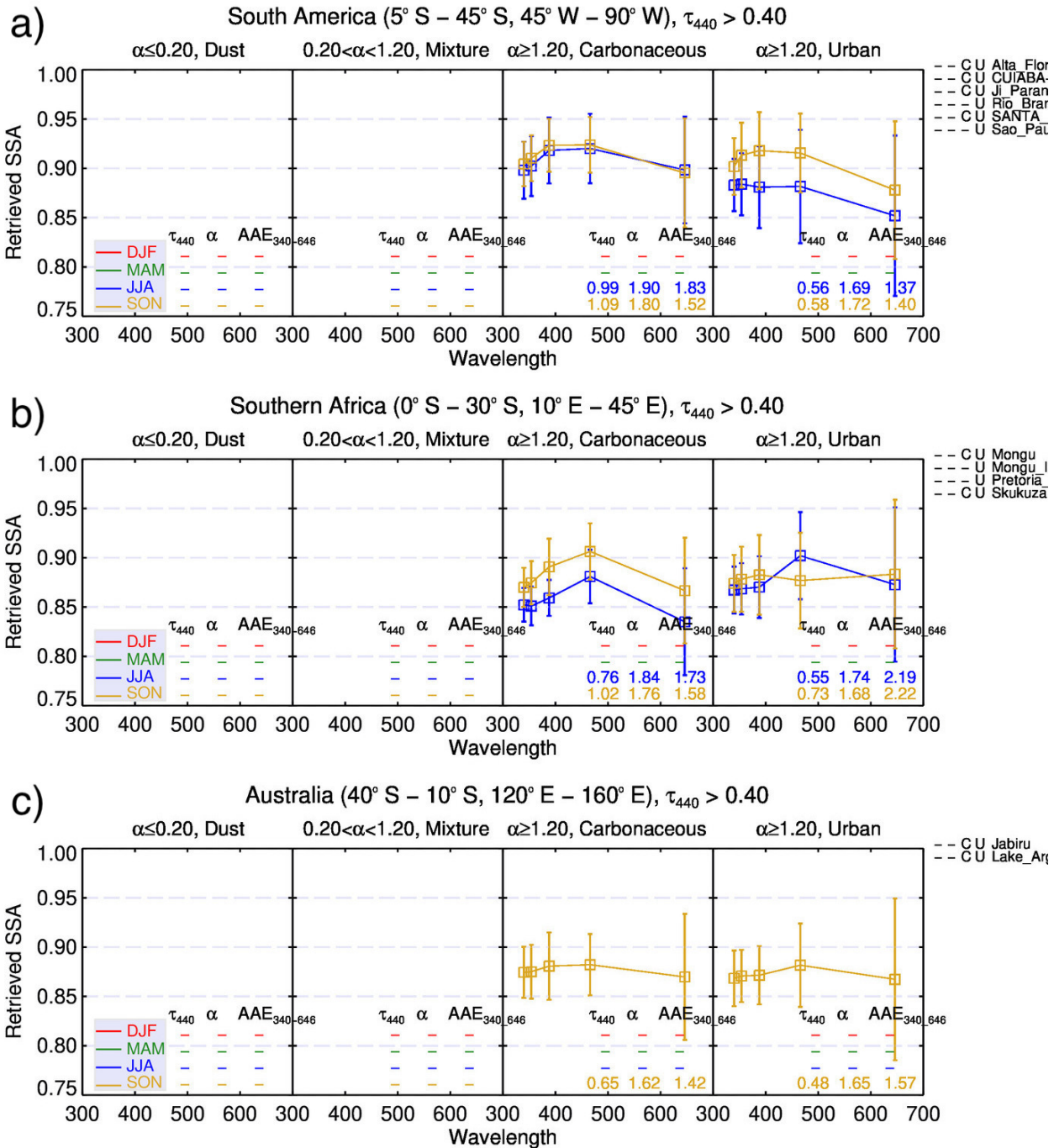
990

Figure 6: Regional average of spectral aerosol SSA derived for observations with $\tau_{440} > 0.4$ over (a) South America, (b) Southern Africa, and (c) Australia. The error bars represent the standard deviation of the observations.
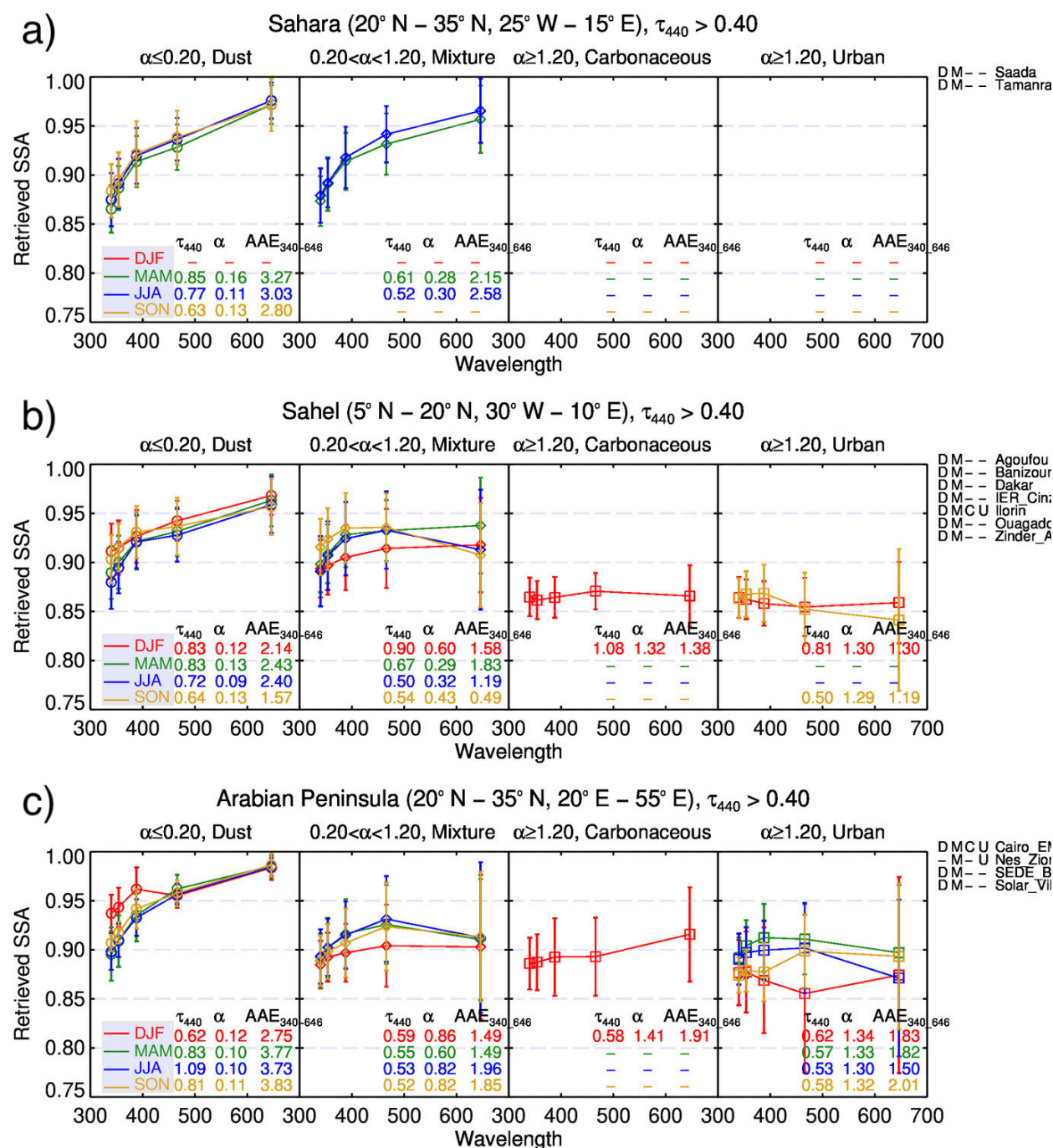
Figure 7: Same as in figure 6 but over (a) Sahara, (b) Sahel, and (c) Arabian Peninsula.

1000
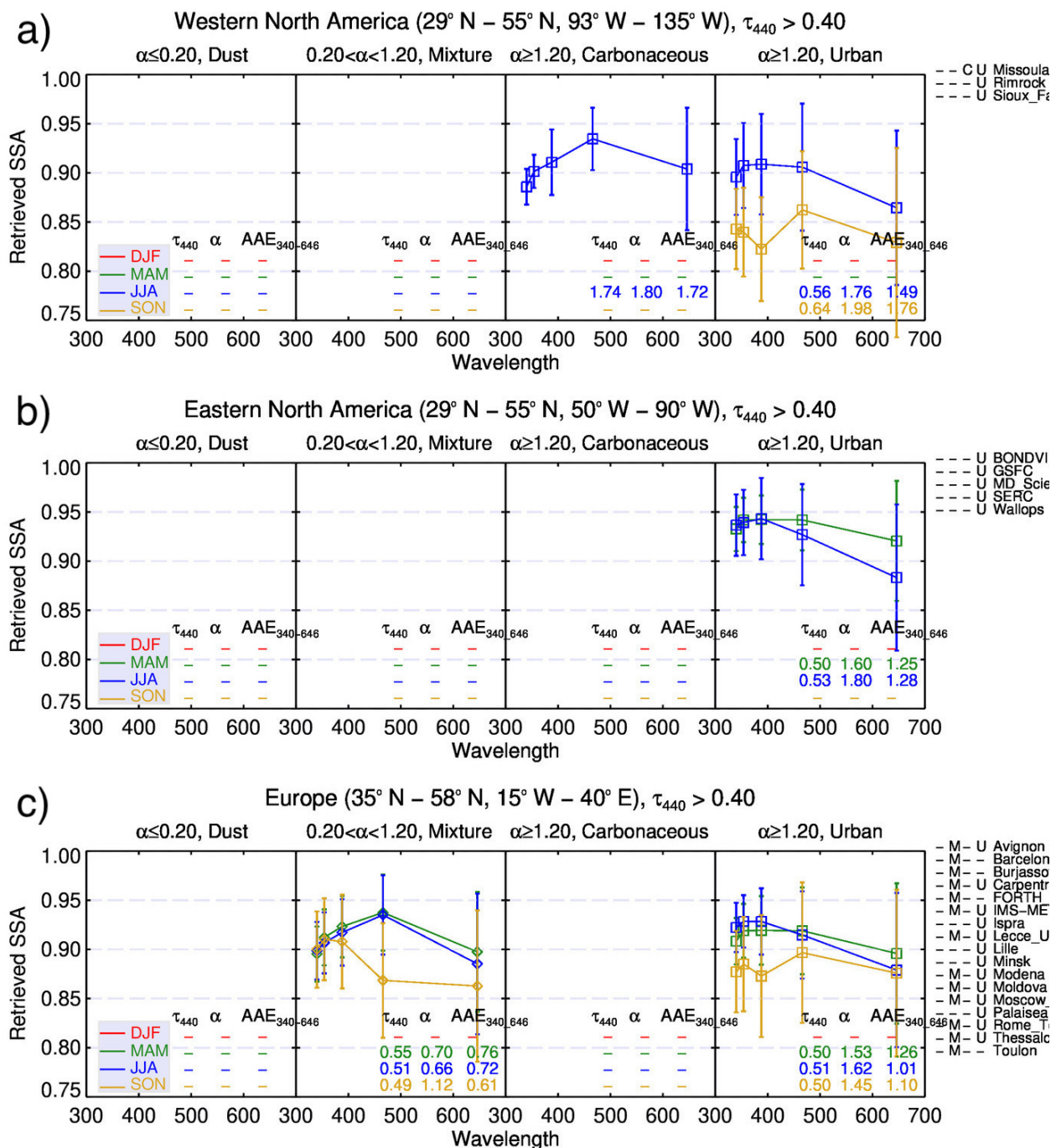
Figure 8: Same as in figure 6 but over (a) Western North America, (b) Eastern North America, and (c) Europe.

1005
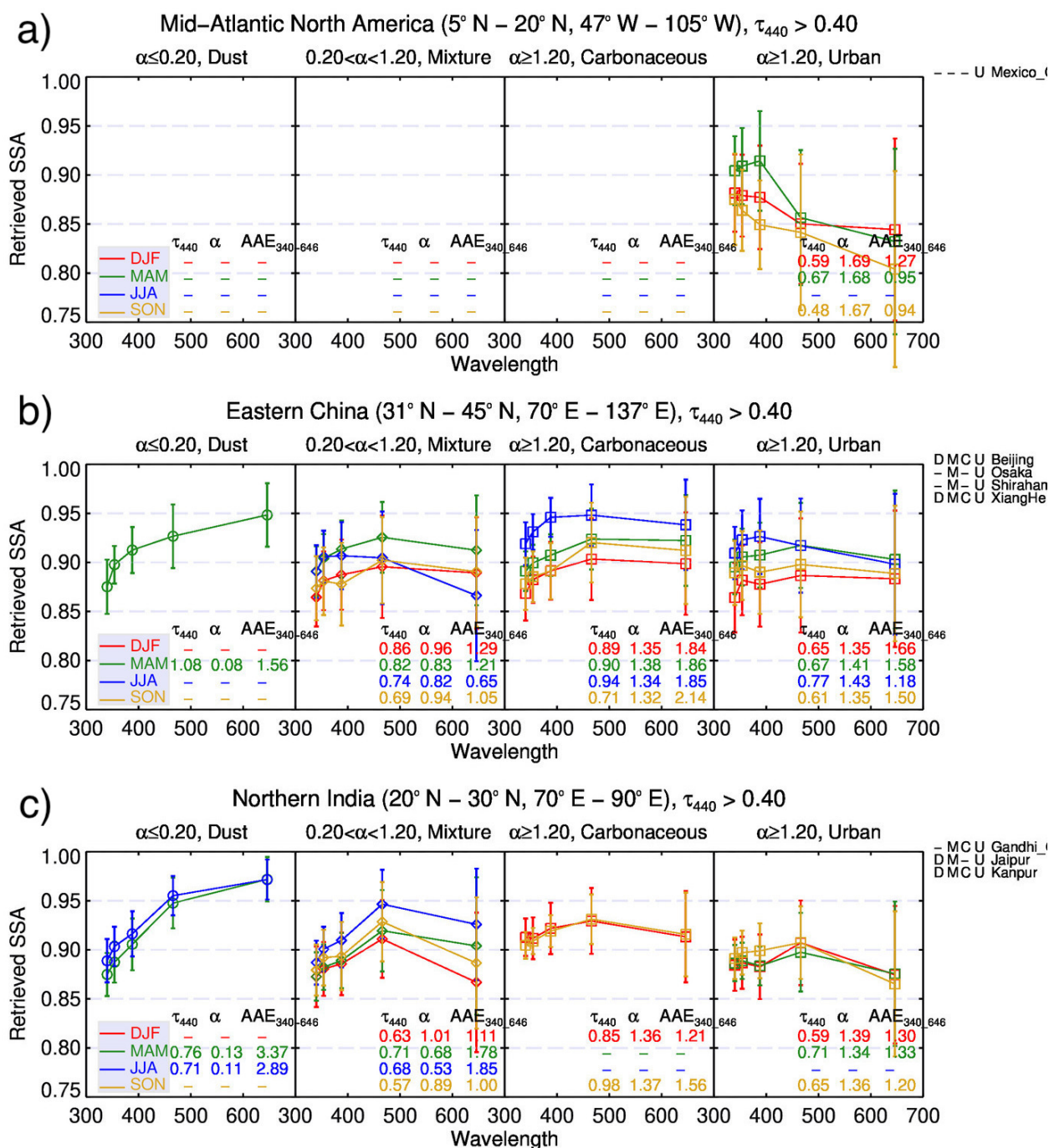
Figure 9: Same as in figure 6 but over (a) Mid-Atlantic North America, (b) North-Eastern Asia, and (c) Northern India.
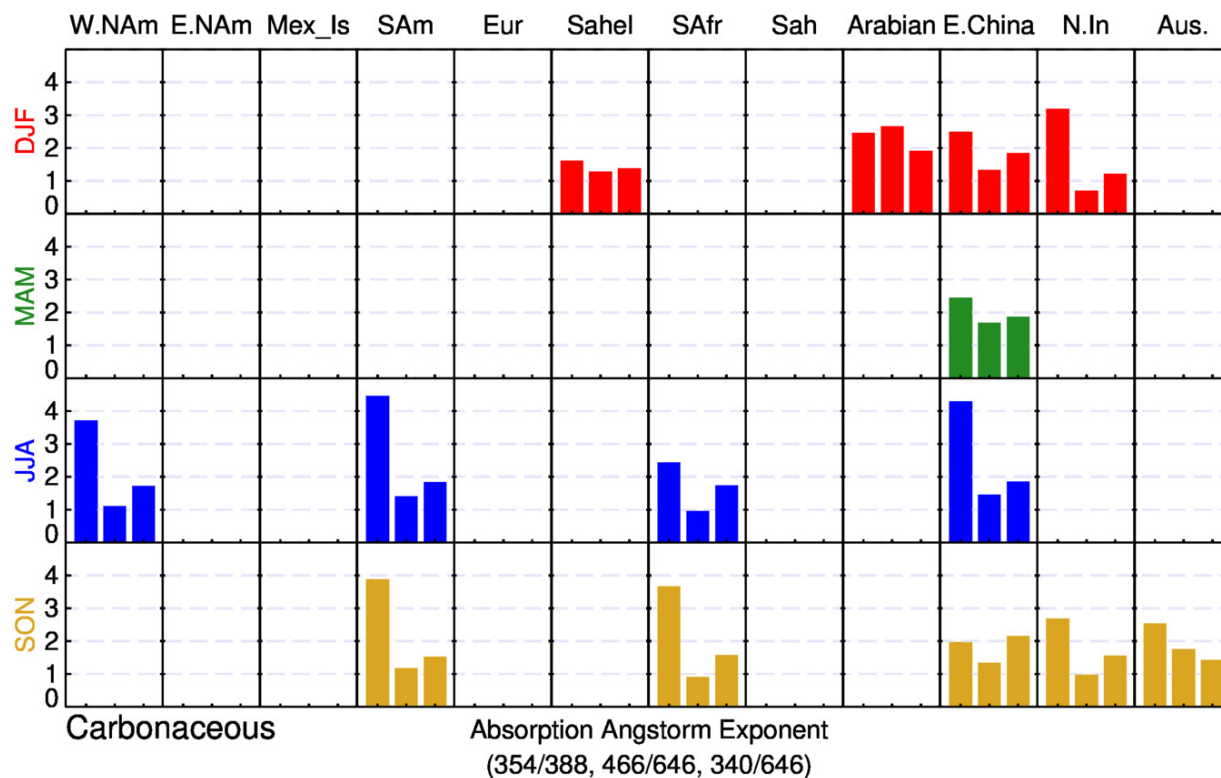
Figure 10: Regional average absorption angstrom exponent at three wavelength pairs from UV-Visible spectrum for Carbonaceous aerosols with $\tau_{440} > 0.4$.
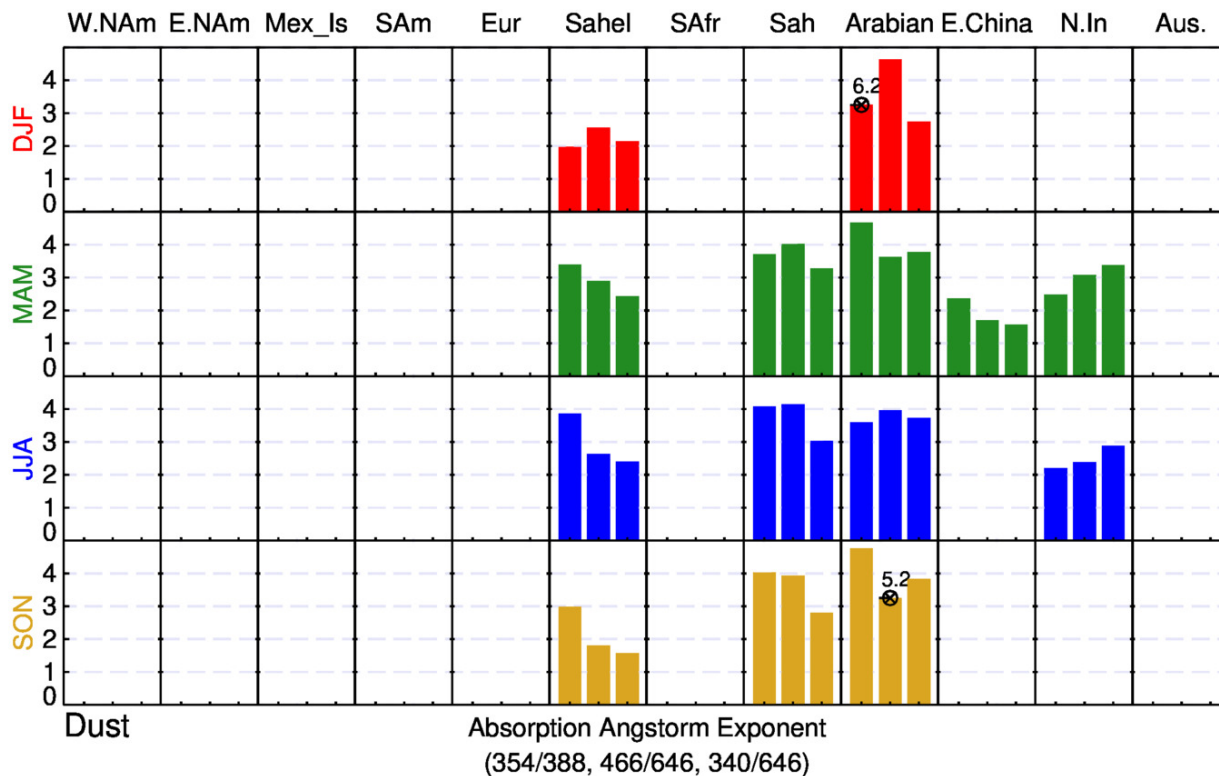
 Figure 11: Same as in figure 10 for Dust aerosols.
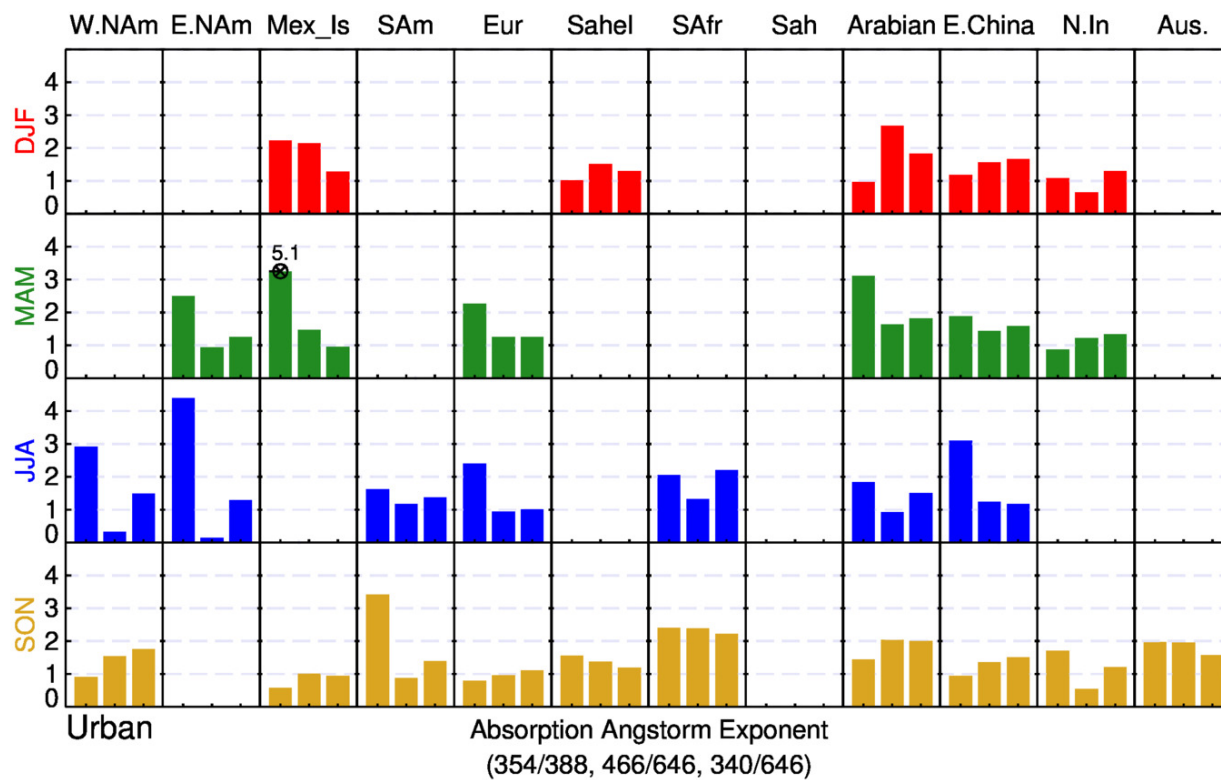
1025 **Figure 12: Same as in figure 10 for Urban aerosols.**
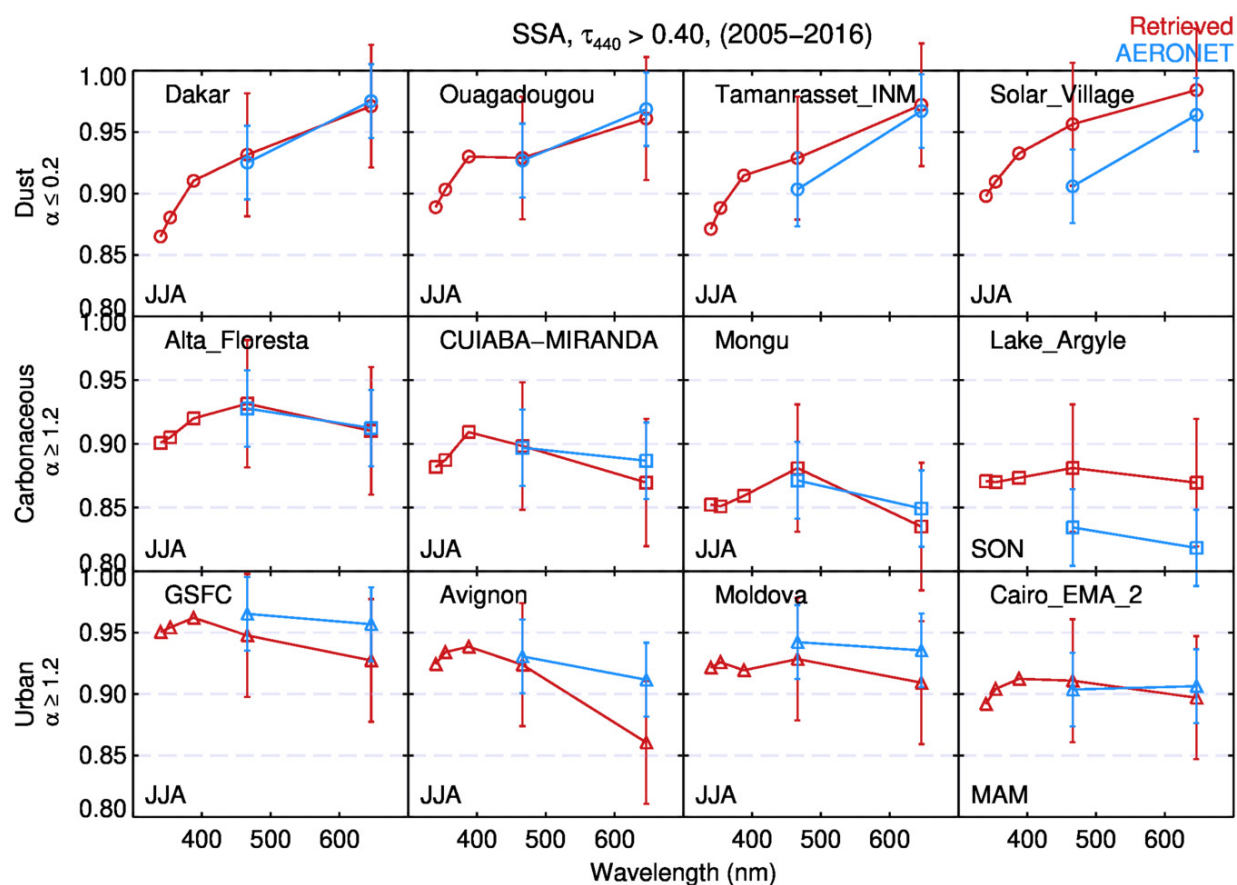
1030

Figure 13: Comparison of retrieved aerosol SSA with that of AERONET for selected sites. The vertical bars represent uncertainty in retrievals – AERONET (±0.03) and the present work (±0.05).

1035
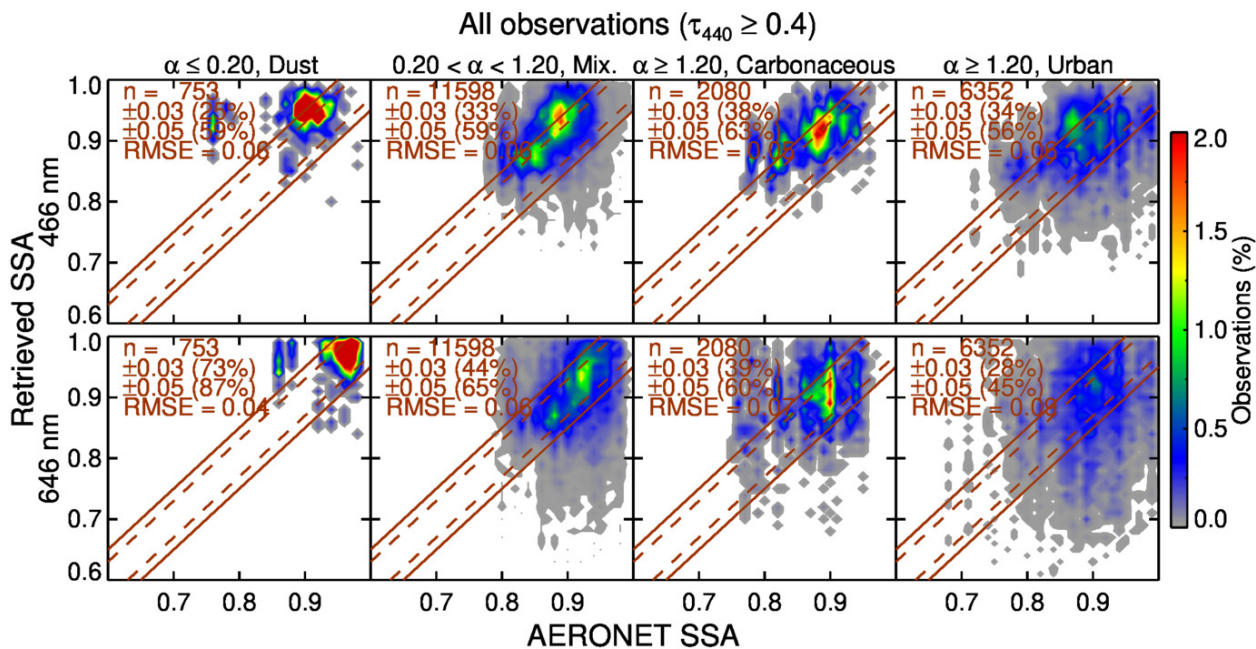
Figure 14: Retrieved SSA versus AERONET at 466 nm and 646 nm for all aerosol types with observations $\tau_{440} > 0.4$.

1040
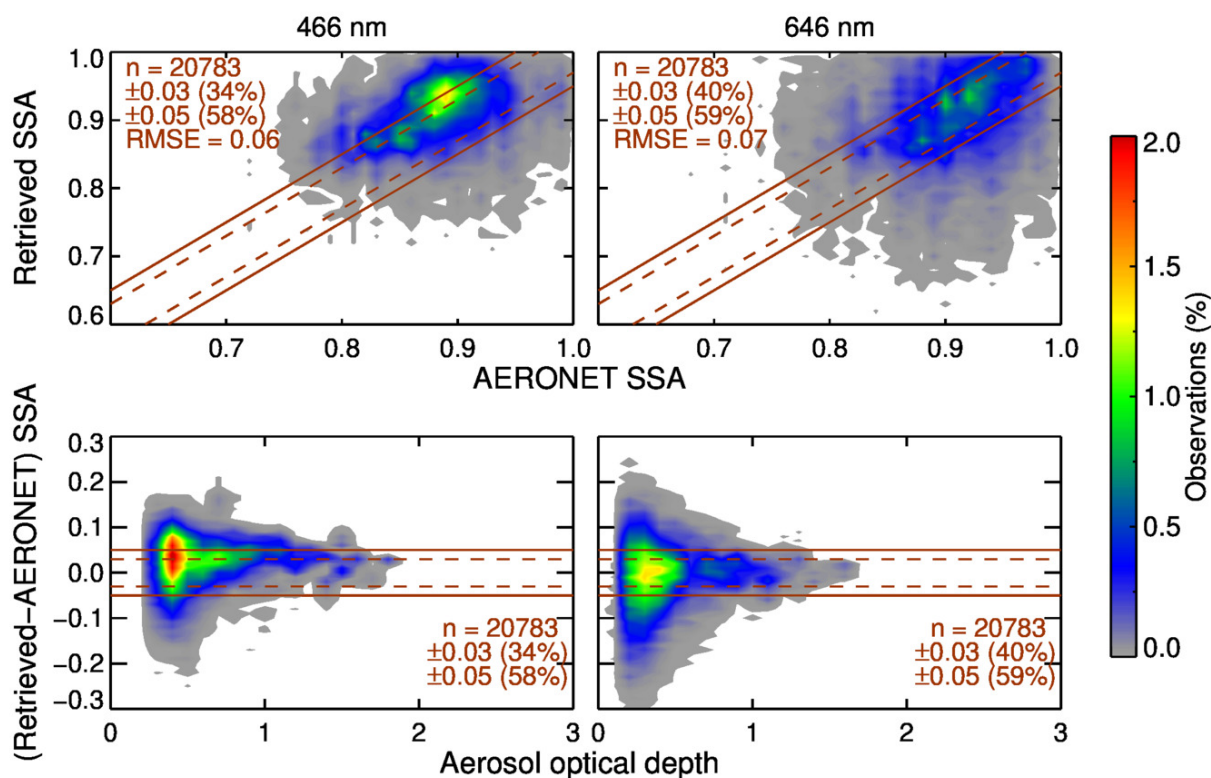
Figure 15: (a) Retrieved SSA versus AERONET, and (b) absolute difference in SSA versus AOD - for observations with $\tau_{440} > 0.4$ and combined aerosol types at 466 nm and 646 nm.